Uncertainty propagation using the Monte Carlo method in the measurement of airborne particle size distribution with a scanning mobility particle sizer

Loïc Coquelin, Laurent Le Brusquet, Nicolas Fischer, François Gensdarmes, Charles Motzkus, Tatiana Macé, Gilles Fleury

▶ **To cite this version:**

Loïc Coquelin, Laurent Le Brusquet, Nicolas Fischer, François Gensdarmes, Charles Motzkus, et al.. Uncertainty propagation using the Monte Carlo method in the measurement of airborne particle size distribution with a scanning mobility particle sizer. Measurement Science and Technology, 2018, 29 (5), 10.1088/1361-6501/aaae87 . hal-01871218

HAL Id: hal-01871218

https://centralesupelec.hal.science/hal-01871218

Submitted on 20 Sep 2018

HAL is a multi-disciplinary open access archive for the deposit and dissemination of scientific research documents, whether they are published or not. The documents may come from teaching and research institutions in France or abroad, or from public or private research centers.

L'archive ouverte pluridisciplinaire **HAL**, est destinée au dépôt et à la diffusion de documents scientifiques de niveau recherche, publiés ou non, émanant des établissements d'enseignement et de recherche français ou étrangers, des laboratoires publics ou privés.

Uncertainty propagation by the Monte-Carlo method in the measurement of airborne particle size distribution with a Scanning Mobility Particle Sizer.

L. Coquelin[1], L. Le Brusquet[2], N. Fischer[1], F. Gensdarmes[3], C. Motzkus[4], T. Mace[4], G. Fleury[2]

[1] *Department of Mathematics and Statistics, National Laboratory of Metrology and Testing, 29 avenue Roger Hennequin, Trappes, 78197, France*

[2] *Laboratoire des Signaux et Systèmes (L2S, UMR CNRS 8506) CentraleSupélec-CNRS-Université Paris-Sud, 3 rue Joliot Curie, Gif-sur-Yvette, 91192, France*

[3] *Institut de Radioprotection et de Sûreté Nucléaire (IRSN), PSN-RES, SCA, LPMA, Gif-sur-Yvette, 91192, France*

[4] *Department of Air quality and Gas Flow Measurement, National Laboratory of Metrology and Testing, 1 rue Gaston Boissier, Paris, 75724, France*

Abstract

Scanning Mobility Particle Sizer (SMPS) is a high resolution nanoparticle sizing system that is widely used as the standard method to measure airborne particle size distributions in the size range 1 nm - 1 μm. This paper addresses the problem to assess the uncertainty associated with the particle size distribution (PSD) when the Differential Mobility Analyzer (DMA) operates under scanning mode. The sources of uncertainty are described and then modeled either through experiments or knowledge extracted from the literature. Special care is brought to model the physics and to account for competing theories. Indeed, it appears that the modeling errors resulting from approximations of the physics can largely affect the final estimate of this indirect measurement especially for quantities that are not measured during the day-to-day experiments. Monte-Carlo method is used to compute the uncertainty associated with the PSD. The method is finally tested against real data sets that are monosize Polystyrene Latex Spheres (PSL) with nominal diameters of 100 nm, 200 nm and 450 nm. The median diameters and associated standard uncertainty of the aerosol particles are estimated as 101.22 nm ± 0.18 nm, 204.39 nm ± 1.71 nm and 443.87 nm ± 1.52 nm with the new approach. Other statistical parameters such as the mean diameter, the mode and the geometric mean and associated standard uncertainty are also computed. These results are finally compared with the results obtained by SMPS embedded software.

Keywords: SMPS measurement, Uncertainty propagation, Monte-Carlo simulations

1. Introduction

Among devices using electrical mobility methods to measure aerosol particle size distribution, the SMPS is the most widely used to characterize particles smaller than 1 μm. It can be applied in fields like: indoors air quality measurement (Kagi et al., 2007), vehicle exhaust pipes (Vogt et al., 2003; Mathis et al., 2004), atmospheric studies (Park et al., 2004), toxicology testing (Oberdörster et al., 2004; Ravenzwaay et al., 2009), etc.. . With the increasing importance of nanomaterials characterization in fundamental research and industrial applications, it is desirable that SMPS measurements are associated with an uncertainty. Indeed, measurement results are commonly expressed in terms of particle diameters (mean, median, mode, ...) calculated from the PSD with an associated standard deviation that simply reflects the measurement

repeatability uncertainty (Motzkus et al., 2013).
An uncertainty analysis in this context could be very useful especially to improve the measurements comparability between laboratories. The GUM and its supplements provide a generic uncertainty evaluation framework that is why the Monte-Carlo method (JCGM 101, 2008) will be used to compute the uncertainty associated with the PSD. Additionally, the paper addresses uncertainty issues that are not currently covered by the GUM: competitive models, functional uncertain inputs, .. . First task is to identify the main contributors to uncertainty. Then, a statistical model will be built for each source if possible (measurements available, literature review, expert opinions, ...) to be finally used in the propagation scheme. Obviously, there are many different ways of building such statistical models and, if more knowledge is available, the models should be updated accordingly or replaced if appropriate. A number of assumptions have been made in the development of the whole measurement model and its associated sources of uncertainty.
The main assumptions are listed below:

- The list of recommendations made by (Chen et al., 2016) is followed throughout the whole presented work. They highlighted in their work that SMPS results are influenced by particle shape and morphology, as well as by the upper and lower size limits set by the instrument (”cutoff” phenomenon at the upper size bound of the SMPS display and counts of ”phantom particles” may be registered around the lower size bound of the SMPS display).

- **particles are spherical**: it is known that nano-sized particles form agglomerates caused by interparticle forces, Van Der Waals as well electrostatic forces especially for combustion sources as power plants and vehicle engines that emit agglomerated particles. These agglomerates produce complex shapes whose morphology is usually characterized by fractal dimension. The charging probability, the penetration efficiencies, and the diffusion of agglomerated particles differ from that of individual spherical particles. All the analysis presented in this work refer to spherical particles only.

- **effects of particles properties (especially chemical composition) are neglected**: the material dependence has proven to yield to slight efficiency curves differences in the size range near the lower detection limit (ISO 27891, 2015). Yet, in the absence of statistical model to account for this source of uncertainty, the effect of particle properties on the CPC detection efficiency is neglected here.

- **sample is considered to be carried in air**: the effect of the carrier gas composition on the CPC detection efficiency is neglected. If the efficiency curves for N_2 and Ar usually coincide that is not the case for all carrier gases, for instance, the efficiencies are generally lower for CO_2 and higher for He.

Taking account of the above assumptions, the results that will be presented in section 5 illustrate the methodology on selected particle sizes larger than 100 nm. Indeed, the uncertainty in the CPC counting efficiency curve becomes negligible above that size. To treat smaller particles using our approach, we recommend to account for that source of uncertainty especially if selected particle sizes are close to the CPC lower detection limit.

Another key point that is essential to address is that the quantity of interest (the measurand) is the airborne PSD entering the DMA inlet. This is why the uncertainty in the aerosol generation as well as in the particles drying operation will not be investigated here. In fact, since SMPS is also used for in-situ measurements (atmospheric research, ...) where the aerosol generation is not controlled, the proposed general framework for uncertainty propagation focuses on the SMPS device.

2. Theoretical background

Differential mobility analysis combines a particle classifier (Differential Mobility Analyzer or DMA) that transmits particles within a narrow interval of mobilities from an initially polydisperse aerosol, and a detector (a Condensation Particle Counter or CPC) that counts the particles within that differential size interval. First, aerosol passes through an inertial impactor to prevent largest particles from entering the DMA column, then, the aerosol enters a charge neutralizer so that particles reach an equilibrium charge state. The particles are then selected by using an electrical classification method inside the column of the DMA: an electric field is created and the airborne particles drift along the column according to their electrical mobility, denoted Z. For a given voltage V, the centroid mobility $Z^*(V)$ for the ideal, non-diffusional transfer function in the cylindrical DMA is given by the following equation

$$Z^*(V) = \frac{(q_{sh} + q_{ex}) \ln\left(\frac{r_2}{r_1}\right)}{4\pi l V}. \tag{1}$$

Matching Z^* with the particle electrical mobility Z_d whose expression is obtained by equating the electric field force with the Stokes drag force,

$$\frac{(q_{sh} + q_{ex}) \ln\left(\frac{r_2}{r_1}\right)}{4\pi l V} = Z^*(V) = Z_d(p, D_p) = \frac{peC_c(D_p)}{3\pi\eta_g D_p}, \tag{2}$$

the particle mobility diameter D_p is the solution of

$$\frac{3(q_{sh} + q_{ex}) \ln\left(\frac{r_2}{r_1}\right)\eta_g}{4lVpe} = \frac{C_c(D_p)}{D_p}, \tag{3}$$

where e is the charge of the electron, p is the number of elementary charges, η_g is the dynamic gas viscosity and C_c is the slip correction that accounts for noncontinuum gas behavior on the motion of small particles and it is given by the following equation

$$C_c(D_p) = 1 + K_n(D_p)\left[a + b\exp\left(-\frac{c}{K_n(D_p)}\right)\right], \quad K_n(D_p) = \frac{2\lambda_m}{D_p}, \tag{4}$$

where (a, b, c) are dimensionless empirical constants so called the slip correction factors, K_n is the Knudsen number and λ_m is the particle mean free path of gas molecules corrected for any temperature and pressure using Willeke's relation

$$\lambda_m = \lambda_{m,0} \times \left(\frac{T}{T_0}\right)^2 \times \left(\frac{P_0}{P}\right) \times \left(\frac{T_0 + S}{T + S}\right), \quad \lambda_{m,0} = 67.3 \text{ nm}. \tag{5}$$

From a known mobility Z^*, the particle mobility diameter D_p can be computed via equation (3) using a root finding algorithm such as the bisection method. The solution is a function of the number of elementary unit of charge the particle carries.

The voltage applied to a scanning DMA varies exponentially (Wang and Flagan, 1990) with time constant τ_v (Collins et al., 2004):

$$V(t) = V_{\min}\exp\left(\pm\frac{t}{\tau_v}\right), \quad \tau_v = \frac{t_s}{\ln\left(\frac{V_{\max}}{V_{\min}}\right)}, \tag{6}$$

where t_s is the scanning time, $V_{\min}$ and $V_{\max}$ are the lower and upper limits of the voltage ramp, respectively.

(Collins et al., 2004) admit in their paper that the most commonly used approach for calculating the particle mobility exiting the DMA is to replace in equation (1) the voltage V by the average voltage $\overline{V}$ the particles

have experienced over their residence time t_f inside the column of the classifier. So, a particle counted at time t was subjected to some voltage $\overline{V(t)}$ whose expression can be derived from equation (6):

$$\overline{V(t)} = \frac{1}{t_f}\int_{t-t_d-t_f}^{t-t_d} V(u)du = \frac{V_{\min}\tau_v}{t_f}\exp\left(\frac{t-t_d}{\tau_v}\right)\left(1-\exp\left(\frac{-t_f}{\tau_v}\right)\right). \tag{7}$$

Assuming that the particle residence time equals the mean fluid residence time inside the column,

$$t_f = \frac{\pi(r_2^2 - r_1^2)l}{q_{sh}+q_a}, \tag{8}$$

The time for particles to pass from the DMA outlet to the detection chamber of the CPC, commonly called the plumbing time, is denoted t_d. It is deduced from the aerosol flow rate, q_a, the plumbing tube diameter, D_{tube}, and length, l_{tube}

$$t_d = \frac{\pi D_{\text{tube}} l_{\text{tube}}}{2q_a}. \tag{9}$$

Knowing the voltage, the corresponding electrical mobility can be calculated using equation (1). Then, the associated particle mobility diameter D_p carrying a given number of elementary charges p is computed via equation (3).

However, the classifier not only selects particles with centroid mobility Z^* but also with slightly higher and lower mobilities, so the selection is modeled with a transfer function ω whose shape is either triangular when aerosol flows are balanced ($q_m = q_a$) or trapezoidal when imbalanced ($q_m \neq q_a$).

(Wang and Flagan, 1990) derived an expression of the non-diffusive transfer function for scanning DMA by choosing the average of the transfer function over the measurement time for every channel.

Yet, for ultra-fine aerosol particles, particle diffusion must be taken into account. On this topic, the work of (Stolzenburg, 1988) stands as a reference because it has been validated through experiments (Jiang et al., 2011) and numerical simulations (Hagwood et al., 1999; Mamakos et al., 2007). This will be discussed later in the section 3.12.

General Model. The instrument response is given as the number of particles counted over time by the CPC. It can be modeled as a set of Fredholm equations. Let k_i be the non-negative kernel function for the time range corresponding to the i^{th} channel (or equivalently for voltage settings corresponding to channel i), $\mathfrak{n}$ the size distribution function that is the number of particles per volume of air with size D_p, $\vec{E}[i]$ the measurement error in the i^{th} channel and $\vec{Y}[i]$ the instrument response (number of particles counted over channel i) commonly modeled as follows

$$\vec{Y}[i] = \int_0^{+\infty} k_i(D_p)\mathfrak{n}(\log(D_p))d(\log(D_p)) + \vec{E}[i], \quad i = 1, ..., I, \tag{10}$$

with

$$k_i(D_p) = q_a t_c[i]\overline{\eta}(D_p)\sum_{p=1}^{+\infty}\phi(p, D_p)\overline{\omega}_i(D_p, p), \tag{11}$$

and

$$\overline{\omega}_i(D_p, p) = \frac{1}{t_c[i]}\int_{t[i]}^{t[i]+t_c[i]}\omega(D_p, p, t)dt, \tag{12}$$

$t[i]$ being the time when the counting for channel i begins (properly adjusted for flow time between the DMA and CPC (Talukdar and Swihart, 2003)) and $t_c[i]$ is the counting time in channel i. $\overline{\eta}(D_p)$ is the bin averages of the efficiency as modeled by (Collins et al., 2002) (cf section 3.10).
The charge distribution on the particles, denoted as $\phi(p, D_p)$ in equation (11), is the probability that a particle of diameter D_p carries p elementary charges. It was fully described by (Fuchs, 1963) and modified afterwards by (Hoppel and Frick, 1986). This expression will be fully detailed in section 3.11.
Actually, only the DMA transfer function ω varies with time in equation (11) and synchronizes the times of the system to relate particle detection to particle selection through the voltage expression. When the DMA voltage is being continuously scanned, the average transfer function over the counting interval $t_c[i]$, denoted $\overline{\omega}_i$, is given by equation (12).
The x-axis is generally discretized to obtain a finite reconstruction problem. If we denote $\left(D_p[j]\right)_{j=1,\dots,J}$ the estimation points, then $n \longmapsto \vec{N} \in \mathbb{R}^J$, with $\vec{N}[j] = \vec{N}(\log(D_p[j]))$ and $k[i, j] = k_i(D_p[j])$. The matrix $\vec{\vec{H}} \in \mathbb{R}^{I\times J}$ is then defined as the discrete evaluation of the integral in equation (10) using Simpson quadrature: let $(\vec{w}[j])_{j=1,\dots,J}$ the weights of the quadrature, then $\vec{\vec{H}}[i, j] = k[i, j]\vec{w}[j]$. Equation (10) is then re-written under matrix form as:

$$\vec{Y} = \vec{\vec{H}}\vec{N} + \vec{E}, \tag{13}$$

where $\vec{Y} \in \mathbb{R}^I$ is the vector of raw data points, $\vec{N} \in \mathbb{R}^J$ is the vector of solution elements and $\vec{E} \in \mathbb{R}^I$ is the vector of measurement errors.

Data Inversion. The inversion of SMPS measurements is to solve an ill-posed problem. Indeed, the stability cannot be guaranteed since matrix $\vec{\vec{H}}$ presents very small singular values and that the subspace in which the noise lives overlaps non trivially with the subspace spanned by the singular vectors of $\vec{\vec{H}}$ (Seinfeld and Wolfenbarger, 1990). To overcome this problem, several methods have been proposed: (Twomey, 1963, 1975; Markowski, 1987; Seinfeld and Wolfenbarger, 1990; Voutilainen, 2001; Collins et al., 2002; Talukdar and Swihart, 2003; Dubey and Dhaniyala, 2013). The scope of this paper is clearly not to describe a new inversion technique, yet, one must set an algorithm to estimate the PSD and we choose to focus on regularization techniques[1]. In this framework, the estimate of the size distribution, denoted as $\hat{\vec{N}}_{[\lambda]}$, is the solution of the following minimization

$$\hat{\vec{N}}_{[\lambda]} = \arg\min_{\vec{N}\geq 0}\left[||\vec{\vec{H}}\vec{N} - \vec{Y}||^2 + \lambda||D_2\vec{N}||^2\right], \tag{14}$$

where D_2 is the second order finite difference matrix used to penalize non-smooth solutions, λ is the regularization parameter and $\vec{N} \geq 0$ means $\vec{N}[j] \geq 0$, $\forall j$. The regularization parameter controls the strength of the prior assumption (here the solutions shall be smooth). (Talukdar and Swihart, 2003) have proposed to estimate λ using a modified L-curve criterion initially developed by (Lawson and Hanson, 1974). Such graphical approach has the benefit that it does not require additional assumptions regarding the noise model. The adaptive pruning algorithm described in (Hansen et al., 2007) is used to compute λ. Other methods can be found in (Phillips, 1962) (discrepancy principle) or (Wahba, 1977) (Generalized Cross Validation).

3. Sources of uncertainty: expressions and modeling

The aim of this section is to bring the users with a procedure to model the contributions of every source to uncertainty. First, all the sources of uncertainty that are suspected to contribute to the variation of the

[1]The uncertainty propagation scheme that will be presented later in the article stays valid regardless of the inversion technique being used to retrieve the PSD.

measurand must be considered. Each source will be either discarded if its contribution to uncertainty is negligible, or, if appropriate, included in the uncertainty budget.

The contribution of some sources to uncertainty can be considerably lowered by specifying convenient experimental settings: increase the sheath flow rate to reduce the particle deposition by diffusion inside the column of the classifier, set an aerosol-to-sheath flow ratio at 0.1, lengthen the scanning time to avoid smearing effect and to ensure a slowly varying voltage ramp. All the precautions are taken to reduce the uncertainty.

Two groups of sources of uncertainty are distinguished: the sources that result in fluctuations of the measured particle count (experimental dispersion) and the modeling errors. Where the experimental dispersion is directly available through the observations (measured particle count), the modeling errors appear when defining the general model, or, more precisely, when building the matrix $\vec{\vec{H}}$ that is needed to estimate the PSD.

The main contribution of this work is to account for the modeling errors, whereas, the common practice is to neglect them by setting a general model with consensual sub-models (bipolar charging law, DMA transfer function, etc.) and to set the model parameters to their nominal values. This approach, although faster, yields to inaccurate estimates of the PSD because it does not account for all the parameters (or functions) fluctuations responsible for the dispersion in the measured signals. Although some of the statistical models presented in this paper may seem pessimistic to the readers, our approach tends to get closer to the true measurement.

Coming sections give a short description of the sources of uncertainty as well as the associated statistical modeling. In the interests of brevity, the models that can be easily found on aerosol textbooks have been moved to annexes. Table 1 lists the considered sources of uncertainty, the associated modeling as well as their respective sections/annexes.

Table 1: List of the considered sources of uncertainty, the associated modeling and their respective sections/annexes.

Source	**Model**	**Section**
Coincidence	Corrected with (Collins et al., 2013)	Appendix A.1
Smearing effect	Corrected with (Collins et al., 2002)	Appendix A.2
CPC counting noise	Non parametric law identified from experiments	section 3.3
Temperature of the carrier gas	Uniform distribution with fixed parameters	Appendix A.3
Pressure of the carrier gas	Uniform distribution with fixed parameters	Appendix A.3
Viscosity of air	Gaussian distribution with fixed parameters	Appendix A.4
DMA geometry	Uniform distribution with fixed parameters	Appendix A.5
DMA voltage	Custom model based on experiments	section 3.7
DMA flow rates	Gaussian distribution with fixed parameters	Appendix A.6
Slip correction factors	Multivariate Gaussian distribution with parameters identified from the literature	section 3.9
Diffusion losses	Corrected with the total penetration efficiency model based on effective lengths from the literature	Appendix A.7
Bipolar charging law	Multivariate Gaussian distribution with parameters identified from the literature	section 3.11
DMA transfer function	Combination of convective and convective-diffusive models	section 3.12
CPC counting efficiency	CPC efficiency curves are taken using air as the sample carrier gas and modeled as error free functions	section 3.13

3.1. Coincidence correction

Please refer to Appendix A.1

3.2. *Smearing effect correction*

Please refer to Appendix A.2.

3.3. *CPC counting noise*

Since the rate of particles entering the CPC occurs at random, the particle count is regularly modeled as a sample drawn from a Poisson process. An experimental verification to ensure that such random process remains accurate for higher concentrations of particles has been performed. Experiments have been carried out with aerosol particles of Di(2-Ethylhexyl) Phthalate (DEHP) for different amounts of dilution (0 to 1000), and so very different levels of concentration. Airborne particles were detected by a Model 3022 CPC manufactured by TSI Incorporated. 40 scans were recorded for each configuration (4 configurations: no dilution, dilution by a factor of 10, 100 and 1000). The mean and the variance of the measured raw count data should be equal to validate the Poisson assumption. Of course, the finite (and reduce) number of scans will not be sufficient to tend to equality but it should be enough to bare a trend. Figure 1 plots the variance of the raw count data as a function of the mean raw count data (each point in the figure, mean and variance being calculated over 40 scans). The results reflect that the Poisson assumption does not hold when the particle concentration is greater than 10^3 cm^{-3}. Indeed, above such concentration, the variance becomes quadratic (logarithm scale) because the CPC no longer operates in single particle count mode. For this reason, raw count data will be modeled as samples drawn from a multivariate normal vector whose parameters will be directly inferred from the measured particle count. This will be described later in the section 4.

Figure 1: Variance of the raw count data as a function of the mean raw count data for 160 scans of DEHP aerosol (40 scans : no dilution; 40 scans : dilution 10; 40 scans : dilution 100; 40 scans : dilution 1000). Every red dot (mean and variance) is computed over 40 scans. The black line stands as the reference Poisson statistic over the whole concentration range.

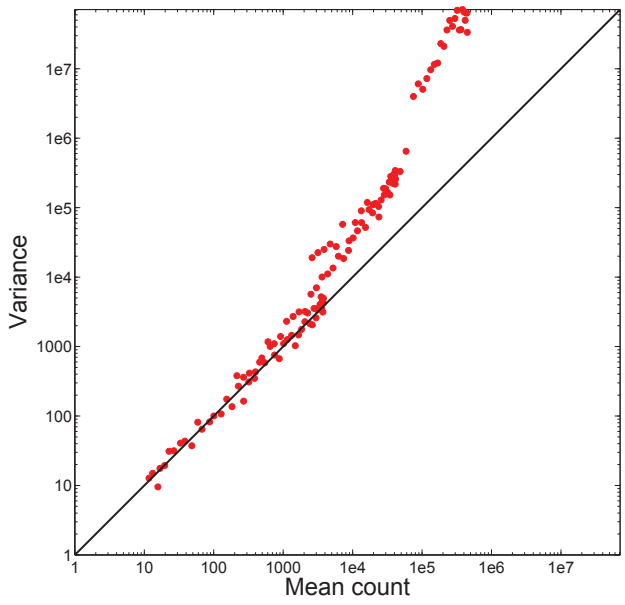

3.4. *Temperature, Pressure*

Please refer to Appendix A.3.

3.5. Viscosity of air

Please refer to Appendix A.4.

3.6. Geometric factors

Please refer to Appendix A.5.

3.7. DMA Voltage

The voltage at the center rod of the DMA scales with the selected particle mobility, so any fluctuation of the voltage tends to broaden the transfer function. Under scanning mode operation, the voltage is continuously increased (equation (6)). To validate this model, a dynamic evaluation of the voltage has been performed and is described in Appendix B.

Statistical Modeling. Because the mean voltage offsets are reasonably low compared with the repeatability uncertainty, the proposed model neglects the bias, and, as a direct consequence, this source of uncertainty will not be included in the uncertainty budget. The new voltage ramp $\hat{V}$ that accounts for the repeatability uncertainty and the input parameters fluctuations between consecutive scans is expressed as follows

$$\hat{V}(t) \quad = \quad \epsilon_V \times V(t, \hat{V}_{min}, \hat{V}_{max}), \tag{15}$$

where

$$\begin{cases} \hat{V}_{min} \sim \mathcal{N}\left(\overline{V_{min}^{AIM}}, \sigma_{V_{min}^{AIM}}\right), \\ \hat{V}_{max} \sim \mathcal{N}\left(\overline{V_{max}^{AIM}}, \sigma_{V_{max}^{AIM}}\right), \\ \epsilon_V \sim \mathcal{U}\left(0.985, 1.015\right). \end{cases} \tag{16}$$

$\overline{V_{min}^{AIM}}$ and $\sigma_{V_{min}^{AIM}}$ refer to the mean and standard deviation of the estimates of V_{min} given by SMPS embedded software. The same goes for $\overline{V_{max}^{AIM}}$ and $\sigma_{V_{max}^{AIM}}$ with the estimates of V_{max}. The uniform random variable ϵ_V scales the voltage ramp. Its minimum and maximum values stand for a relative uncertainty value of 1.5 %. This model only applies for scanning times longer than 120 s.

3.8. DMA flow rates

Please refer to Appendix A.6.

3.9. Slip correction factors

The Cunningham slip correction factor C_c is used to correct Stokes's law for the fact that the no-slip boundary condition is violated for small aerosol particles moving with respect to the gaseous medium (Allen and Raabe, 1985). The Knudsen-Weber form of the slip correction is given by equation (4).
Table 2 summarizes several published values for the empirical constants a, b and c. Considering the traceability of the experiments, standard (ISO 15900, 2009) recommends the use of the coefficients determined by (Kim et al., 2005) for particle size measurements. It also points out that the results of the experiments led by (Allen and Raabe, 1985) closely agree with those of (Hutchins et al., 1995). Quite recently, (Jung et al., 2012) have re-evaluated the coefficients determined by (Kim et al., 2005) using the current smallest SRM®1964 and have found a new value for $c = 1.001$.

Table 2: Some published values of Slip correction factors for Stokes' law (Standard (ISO 15900, 2009))

Authors \ Parameters	$\lambda_{m,0}$ [nm]	a	b	c
Knudsen and Weber (1911)	94.17	0.772	0.400	1.630
Millikan (1923b)	94.17	0.864	0.290	1.250
Davies (1945)	66.00	1.257	0.400	1.100
DeMarcus, Thomas (1952)	65.50	1.250	0.440	1.090
Reif (1958)	65.20	1.260	0.450	1.080
Fuchs (1964)	65.30	1.246	0.420	0.870
Dahneke (1973)	66.00	1.234	0.414	0.870
Allen et Raabe (1982)	67.30	1.155	0.471	0.596
Allen et Raabe (1985)	67.30	1.142	0.558	0.999
Rader (1990)	67.40	1.207	0.440	0.780
Hutchins *et al.* (1995)	67.30	1.231	0.4695	1.1783
Kim *et al.* (2005)	67.30	1.165	0.483	0.997
Jung *et al.* (2012)	67.30	1.165	0.480	1.001

Statistical Modeling. a, b and c are modeled as samples drawn from the truncated normal distributions A, B and C, respectively. Let $\theta_{A,B,C} = \begin{pmatrix} A \\ B \\ C \end{pmatrix}$, a multivariate truncated normal vector and $C_c(D_p;\theta_{A,B,C})$, the slip correction calculated at diameter D_p with the empirical constants drawn from $\theta_{A,B,C}$. Four sets of coefficients are used to model A, B and C: $\theta^A_{A,B,C} = \begin{pmatrix} a_A \\ b_A \\ c_A \end{pmatrix}$, $\theta^H_{A,B,C} = \begin{pmatrix} a_H \\ b_H \\ c_H \end{pmatrix}$, $\theta^J_{A,B,C} = \begin{pmatrix} a_J \\ b_J \\ c_J \end{pmatrix}$, and $\theta^K_{A,B,C} = \begin{pmatrix} a_K \\ b_K \\ c_K \end{pmatrix}$ [2]. Mean values for A, B and C are set as the coefficients of (Jung et al., 2012). Indeed, it is the most recent study that brings us with traceable results. The other sets will be used for the truncation as shown below.

$$\theta_{A,B,C} \sim \mathcal{N}_{[\theta^{\text{low}}_{A,B,C},\theta^{\text{up}}_{A,B,C}]}(\theta^{\text{mean}}_{A,B,C}, \Sigma_{\theta_{A,B,C}}), \tag{17}$$

$$\theta^{\text{low}}_{A,B,C} = \begin{pmatrix} a_A \\ b_H \\ c_K \end{pmatrix} = \begin{pmatrix} 1.142 \\ 0.4695 \\ 0.997 \end{pmatrix}, \quad \theta^{\text{mean}}_{A,B,C} = \begin{pmatrix} a_J \\ b_J \\ c_J \end{pmatrix} = \begin{pmatrix} 1.165 \\ 0.480 \\ 1.001 \end{pmatrix}, \quad \theta^{\text{up}}_{A,B,C} = \begin{pmatrix} a_H \\ b_A \\ c_H \end{pmatrix} = \begin{pmatrix} 1.231 \\ 0.558 \\ 1.1783 \end{pmatrix}.$$

The covariance matrix $\Sigma_{\theta_{A,B,C}}$ is defined as follows [3]:

$$\Sigma_{\theta_{A,B,C}} = \text{diag}\left(\max\left(|\theta^{\text{mean}}_{A,B,C} - \theta^{\text{low}}_{A,B,C}|^2, |\theta^{\text{up}}_{A,B,C} - \theta^{\text{mean}}_{A,B,C}|^2\right)\right). \tag{18}$$

The covariances are neglected here (the covariance matrix $\Sigma_{\theta_{A,B,C}}$ is diagonal). Moreover, the variances are voluntary increased compared to (Jung et al., 2012) because the coefficients are not estimated during the

[2] Superscripts A, H, J and K refer to (Allen and Raabe, 1985), (Hutchins et al., 1995), (Jung et al., 2012) and (Kim et al., 2005), respectively.

[3] $\text{diag}\,(\max\,(\text{Vector1}, \text{Vector2})) := \begin{bmatrix} \max\,(\text{Vector1}[1], \text{Vector2}[1]) & 0 & \dots & 0 \\ 0 & \max\,(\text{Vector1}[2], \text{Vector2}[2]) & \dots & 0 \\ & & \ddots & \\ 0 & 0 & & 0 \\ 0 & 0 & \dots & \max\,(\text{Vector1}[n], \text{Vector2}[n]) \end{bmatrix}$

experiment and, by definition, will not be updated.
Figure 2 gives some realizations of the relative difference to Jung's correction for the authors listed in table 2. The relative difference lies within +3% and −4% in the diameter range 1 nm–1 μm. It also shows the relative difference to some realizations of $C_c(D_p;\theta_{A,B,C})$. The proposed statistical modeling appears to reach a consensual solution to model the current knowledge.

Figure 2: Relative difference to (Jung et al., 2012) correction for the authors listed in table 2 as well as the relative difference to some realizations of $C_c(D_p;\theta_{A,B,C})$ (grey curves) over the particle range 1 nm–1 μm.

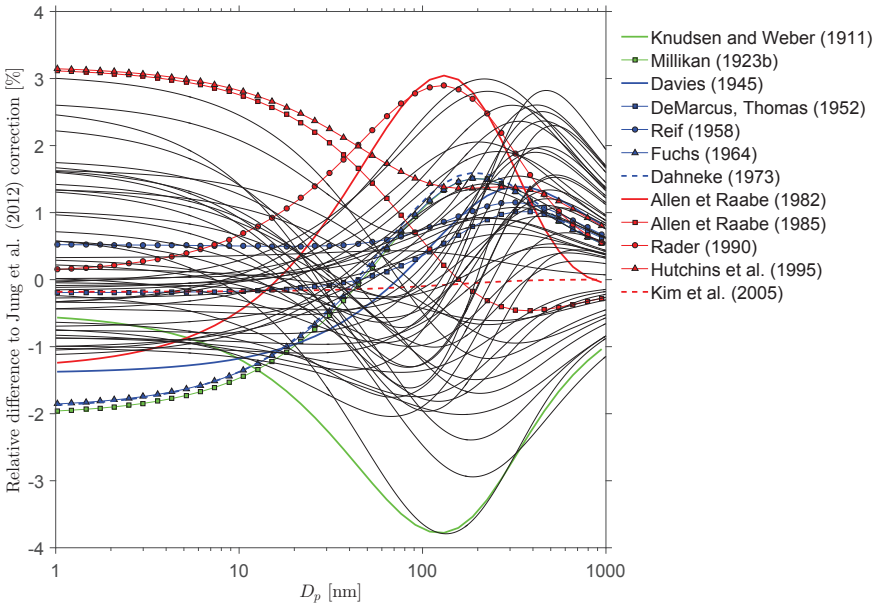

3.10. *Diffusion losses*

Please refer to Appendix A.7.

3.11. *Bipolar charging law*

The approximation of (Wiedensohler, 1988) derived from (Fuchs, 1963), simple and fast, is the most commonly used approach to compute the charge distribution function. Nevertheless, standard (ISO 15900, 2009) considers that an expert user of DMAs should be able to calculate ϕ as described by (Fuchs, 1963). For this reason, to derive the uncertainty associated with ϕ, starting with Fuchs original theory seems to be the best approach.
Two widely accepted approaches exist for treating diffusion charging of aerosol particles in the transition regime: the limiting-sphere theory and approximate solutions of the Boltzmann equation. The limiting-sphere theory assumes two regions separated by an imaginary sphere concentric to the particle. Between this sphere and the particle surface, motion of the ions is determined by the thermal speed and interaction potential with the particle, while outside the sphere, this is described by the macroscopic diffusion-mobility theory (for more details, see (Reischl et al., 1996) and (Biskos, 2004)). Fuchs, matching the two fluxes at the surface of the limiting-sphere, derived an expression of the bipolar charging law such that

$$\phi(p,D_p) = \begin{cases} \dfrac{\prod_{p=+1}^{+\infty}\left(\frac{\beta_{p-1}^{+}}{\beta_{p}^{-}}\right)}{\Upsilon} & ,\text{if } p \geq 1, \\ \dfrac{\prod_{p=-1}^{-\infty}\left(\frac{\beta_{p+1}^{-}}{\beta_{p}^{+}}\right)}{\Upsilon} & ,\text{if } p \leq -1, \\ \frac{1}{\Upsilon} & ,\text{if } p = 0, \end{cases} \tag{19}$$

where

$$\Upsilon = \sum_{p=+1}^{+\infty}\left[\prod_{p=+1}^{+\infty}\left(\frac{\beta_{p-1}^{+}}{\beta_{p}^{-}}\right)\right] + \sum_{p=-1}^{-\infty}\left[\prod_{p=-1}^{-\infty}\left(\frac{\beta_{p+1}^{-}}{\beta_{p}^{+}}\right)\right] + 1. \tag{20}$$

Fuchs calculations are based on the definition of the ion-aerosol attachment coefficients $\beta_p^{\pm}$. See Appendix C for the calculations of these coefficients. To compute the bipolar charging law, the ionic properties of the carrier gas must be known, namely the electrical mobilities and the masses of small ions (positive and negative), denoted as z_I^+, z_I^-, m_I+ and m_I^-, respectively.

Table 3 gives some published values of the ionic properties for dry air. It reflects that large differences exist within the authors especially for the masses of small ions (m_I^- stands between 50 and 140 amu and m_I^- stands between 109 and 290 amu). (Wiedensohler, 1988) uses a fixed ratio for ion mobilities z_I^+/z_I^- equal to 0.875 whereas the computed ratios for the various authors listed in table 3 belong to the interval $[0.7228; 0.8889]$.

Table 3: Some published values of the ionic properties for dry air.

Authors \ Parameters	z_I^+ [amu]	z_I^- [amu]	m_I+ [amu]	m_I^- [amu]
Vohra (1969)	1.40	1.90	109	50
Mohnen (1977)	1.40	1.90	130	100
Postendörfer et al. (1983)	1.15	1.39	140	101
Wen et al. (1984)	1.40	1.90	130	130
Hoppel and Frick (1986)	1.20	1.35	150	90
Wiedensohler et al. (1986)	1.35	1.60	148	130
Hoppel and Frick (1990)	1.33	1.84	200	100
Wiedensohler and Fissan (1991)	1.40	1.60	140	101
Reischl et al. (1996)	1.15	1.425	290	140

Statistical Modeling. For a known quadruplet $(z_I^+, z_I^-, m_I^+, m_I^-)$, ϕ can be computed for any particles with diameter D_p carrying p charges ($K = 9$ quadruplets from table 3). First approach to model the bipolar law is to sample as many quadruplets as necessary[4] and to compute the associated ϕ. However, calculating ϕ for a given quadruplet is time consuming that is why a more effective solution is preferable. Our concern is that the proposed statistical modeling, first, preserves the spatial correlations, and, second, accounts for the various options available to model the ionic properties. To fulfill these requirements, ϕ is modeled as a sample drawn from a multivariate Gaussian distribution Φ_p whose parameters are directly estimated through the disposable data set. The currently available information can be summarized within a $J \times K$ matrix that contains the sampled J-dimensional vectors $\phi_k(p, D_p)$, where $\phi_k(p, D_p)$ is the bipolar charging law calculated with the k^{th} quadruplet from table 3.

Let $\Phi_{p,\text{samp}}$ be this matrix, it can be written as follows

$$\Phi_{p,\text{samp}} = \begin{bmatrix} \phi_1(p, D_p[1]) & \phi_2(p, D_p[1]) & \dots & \phi_k(p, D_p[1]) & \dots & \phi_K(p, D_p[1]) \\ \phi_1(p, D_p[2]) & \phi_2(p, D_p[2]) & \dots & \phi_k(p, D_p[2]) & \dots & \phi_K(p, D_p[2]) \\ \vdots & \vdots & & \vdots & & \vdots \\ \phi_1(p, D_p[J]) & \phi_2(p, D_p[J]) & \dots & \phi_k(p, D_p[J]) & \dots & \phi_K(p, D_p[J]) \end{bmatrix}. \tag{21}$$

Let $\mu_{\Phi_{p,\text{samp}}}$ and $\sigma_{\Phi_{p,\text{samp}}}$ the J-dimensional mean vector and standard deviation vector of $\Phi_{p,\text{samp}}$, respectively. These quantities are computed as follows

$$\mu_{\Phi_{p,\text{samp}}}[j] = \frac{1}{K}\sum_{k=1}^{K}\Phi_{p,\text{samp}}[k, j], \quad \sigma_{\Phi_{p,\text{samp}}}[j] = \sqrt{\frac{1}{K-1}\sum_{k=1}^{K}\left(\Phi_{p,\text{samp}}[k, j] - \mu_{\Phi_p^{\text{samp}}}[j]\right)^2}, \quad j = 1, ..., J. \tag{22}$$

[4] A large amount here since the Monte Carlo method is used to propagate the uncertainty through the all system

Let $C_{\Phi_{p,\text{samp}}}$ the $J \times J$ matrix containing the pairwise Pearson's linear correlation coefficient between each pair of columns in the matrix $\Phi^T_{p,\text{samp}}$. Using a SVD decomposition, $C_{\Phi_{p,\text{samp}}}$ can be written as $C_{\Phi_{p,\text{samp}}} = U_{C_{\Phi_{p,\text{samp}}}} \Sigma_{C_{\Phi_{p,\text{samp}}}} U^T_{C_{\Phi_{p,\text{samp}}}}$. A new J-dimensional random vector ϕ_p, distributed as a multivariate normal distribution Φ_p, can then be obtained

$$\phi_p = \mu_{\Phi_{p,\text{samp}}} + \left(U_{C_{\Phi_{p,\text{samp}}}} \Sigma^{\frac{1}{2}}_{C_{\Phi_{p,\text{samp}}}} z \right) \circ \sigma_{\Phi_{p,\text{samp}}}, \tag{23}$$

where $\circ$ refers to the Hadamard product or element-wise product and z is sampled from $\mathcal{Z}$ with $\mathcal{Z} \sim \mathcal{N}(0, \vec{I}_J)$.

Such formulation has the benefit to account for the dispersion among listed authors regarding the values of the ionic properties via the expression of $\sigma_{\Phi_{p,\text{samp}}}$. Moreover, it maintains the correlation structure between consecutive discrete function evaluations (realistic transition between $\phi_p[j]$ and $\phi_p[j+1]$ for all j) via the definition of $C_{\Phi_{p,\text{samp}}}$.

Figure 3 shows the set of bipolar charging laws calculated from the list of published quadruplets in table 3. It also prints the computed 95 % confidence region associated with Φ_1 over the all diameter range. The developed model seems a convenient way to express the many options available from the literature. On the other hand, these approach may seem quite conservative to the readers (high dispersion of ϕ_p for a given diameter), but, since the ionic properties are not measured during the day-to-day experiments, they will not be updated.

Figure 3: Bipolar charging law $\phi(p = 1, D_p)$ for various ionic properties (cf table 3) in the size range 1 nm–1 μm and the 95 % confidence region associated with Φ_1 computed over 50 000 samples.

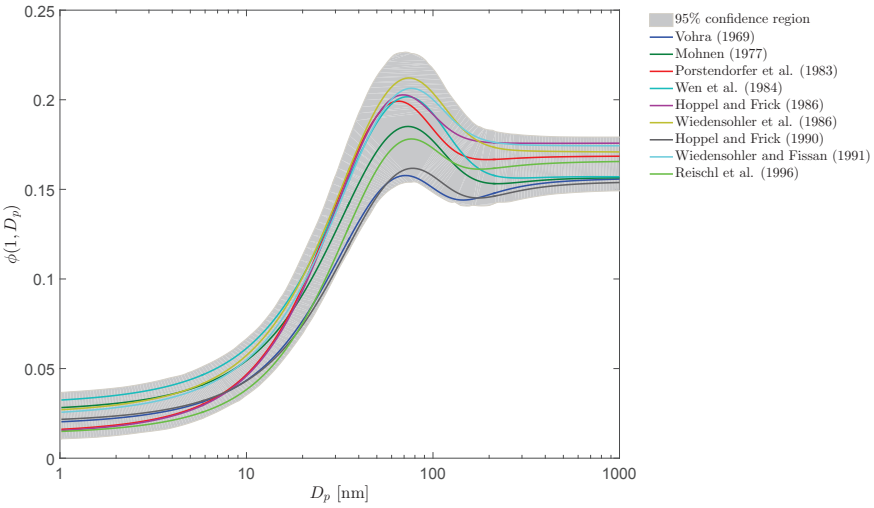

3.12. DMA transfer function

To derive the expression of the DMA transfer function operating in scanning mode, the convection-diffusion equation that models the motion of a particle subject to Brownian motion through an electric field must be solved. DMA selects particles in the size range 1 nm – 1 μm and it is well known that diffusion is the primary transport mechanism for particles smaller than 100 nm. The larger the particles, the less meaningful the diffusive transport.

Two models for the transfer function are investigated: the convective and the convective-diffusive. If most

algorithms set one model for the DMA transfer function, our approach combines convective and convective-diffusive models. See Appendix D for the expressions of ω_{nd} (non-diffusive model) and ω_d (diffusive model).

Statistical modeling. The diffusive transfer function ω_{d} properly models the diameter range 1 nm – 100 nm and the ideal transfer function ω_{nd} commonly codes for particles larger than 100 nm. To cover the whole diameter range, both theories can be combined. In fact, the transition from convective-diffusive to convective transport is purposefully made smoother by defining g, a continuous and regular function[5], and a random threshold $D_{p,\mathrm{thres}}$ that represents the diameter above which the convective transport will progressively (linear transition) replace the convective-diffusive transport. So, ω is defined as a combination of ω_{d} and ω_{nd} via the following expression

$$\omega = g(D_p)\omega_{\mathrm{nd}} + (1 - g(D_p))\omega_{\mathrm{d}}, \tag{24}$$

where g is given by

$$g(D_p) = \begin{cases} 0 & , \text{ if } D_p \leq D_{p,\mathrm{thres}}, \\ 1 & , \text{ if } D_p \geq D_{p,\mathrm{thres}} + \Delta_{\mathrm{thres}}, \\ \frac{D_p - D_{p,\mathrm{thres}}}{\Delta_{\mathrm{thres}}} & , \text{ if } D_p \in]D_{p,\mathrm{thres}}, D_{p,\mathrm{thres}} + \Delta_{\mathrm{thres}}[, \end{cases} \tag{25}$$

and

$$D_{p,\mathrm{thres}} \sim \mathcal{U}[D^{\mathrm{low}}_{p,\mathrm{thres}}, D^{\mathrm{up}}_{p,\mathrm{thres}}], \tag{26}$$

where Δ_{thres}, $D^{\mathrm{low}}_{p,\mathrm{thres}}$ and $D^{\mathrm{up}}_{p,\mathrm{thres}}$ are set to 100, 100 and 400 nm, respectively. $D_{p,\mathrm{thres}}$ is modeled as a uniform random variable to account for the uncertainty in the location of the exact transition between the two regimes. Of course, one can discuss the range of variation of $D_{p,\mathrm{thres}}$. Additionally, ω depends on several parameters (flow rates, electrical mobility, ...) via the expressions of ω_{nd} and ω_{d}, parameters that will be drawn from their respective distributions as detailed throughout the section 3.

3.13. CPC counting efficiency

The primary parameter of interest when evaluating the performance of CPCs is particle detection efficiency as a function of particle diameter. (Scheibel and Porstendörfer, 1983) described the measurement method that has usually been used to determine particle detection efficiency: particle concentration measurements made by CPCs are compared with aerosol electrometer measurements (Faraday cup electrometer) of singly charged particles. In most experiments, the nearly monodispersed aerosol is produced by using a Scheibel-Porstendörfer generator (or a Bartz et al. generator (Bartz et al., 1987)) with an electrostatic classifier (DMA).

The CPC detection efficiency mainly depends on the particle number concentration, the particle size, and the particle composition. Moreover, there are slight differences in the efficiency curves of each instrument (instrument to instrument variation), the working fluids (water or alcohol) exhibit some material dependence and the carrier gas composition affects the efficiency.

Indeed, the dependence of the detection efficiency of CPCs on the particle properties has been shown by several authors, especially on the chemical composition of sampled particles. The material dependence was

[5]Continuity and regularity will ensure a smooth transition between the two regimes which seems to be much closer to the physics.

studied mainly with sodium chloride and silver. Some difference in the detection efficiency was observed in the size range near the lower detection limit, and silver seemed to show slightly higher detection efficiencies than sodium chloride. More recent work with 1-butanol-based CPCs investigated a wider variety of materials which showed that oils were easiest to detect while inorganic salts were hardest (ISO 27891, 2015).

The effect of the carrier gas composition on the detection efficiency was studied by (Niida et al., 1988) where he investigated the counting efficiency of CPCs using N_2, Ar, CO_2 and He. He noted slight efficiency curve differences: the efficiency curves for N_2 and Ar usually coincide, He leads to higher efficiencies and, for CO_2, the efficiencies are generally lower.

Later, (Sem, 2002) reviewed available data describing the performance of TSI 3010, 3022A and 3025A CPCs. He summarized the data reported in the literature including the sources of uncertainty coming from the response time for step increase and step decrease of aerosol concentration, the effects on detection efficiency of RH of 0-50 % and the dependence of counting efficiency on input particle concentration.

As a reminder, one of the main assumption used in this work is that the sample is considered to be carried in air. Furthermore, as far as we know, no statistical model is available to account for the CPC measurement uncertainty and, assessing such uncertainty is out of the scope of this paper. For that reason, the CPC efficiency curves are taken using air as the sample carrier gas and modeled as error free functions. Aware of this limitation, the results shown in section 5 refer to selected particle sizes very much larger (100 nm PSL, 200 nm PSL and 450 nm PSL) than the lower detection limit making these listed sources of uncertainty less meaningful.

4. Propagation of the sources via Monte-Carlo simulations

The proposed approach to propagate the sources of uncertainty is based on the Monte Carlo method. It can be referred to as a two-stage approach: the first stage models the experimental dispersion and the second stage handles the modeling errors. In practice, several scans are collected. Since the quantity to be characterized varies over time, it is crucial to ensure that the aerosol remains stable during the experiment. The stability is not quantified here, but, the experimentalists have to check whether the fluctuations among samples are kept reasonably low.

First, the measured particle count is corrected for coincidence and smearing. Then, depending on the number of scans available, the measured raw count data $\vec{Y}$ are either modeled as samples drawn from a multivariate Poisson distribution ($N_{scans} = 1$) or as samples drawn from a multivariate Gaussian distribution ($N_{scans} > 1$). In the case where $N_{scans} > 1$, let $C_{\vec{Y}}$ be the measured samples empirical correlation matrix, $\mu_{\vec{Y}}$ and $\sigma_{\vec{Y}}$ the measured particle count mean vector and standard deviation vector. $C_{\vec{Y}}$ can be decomposed by SVD (Singular Value Decomposition) such that $C_{\vec{Y}} = U_{C_{\vec{Y}}} \Sigma_{C_{\vec{Y}}} U_{C_{\vec{Y}}}^T$. Then, the simulated raw count data samples $\tilde{\vec{y}}$ are sampled

$$\tilde{\vec{y}} = \mu_{\vec{Y}} + \left(U_{C_{\vec{Y}}} \Sigma_{C_{\vec{Y}}}^{\frac{1}{2}} z \right) \circ \sigma_{\vec{Y}}, \tag{27}$$

by drawing as many samples of z, with $z \sim \mathcal{N}(0, \vec{\vec{I}}_I)$, $\vec{\vec{I}}_I$ being the unit matrix of size I. The experimental dispersion (fluctuations of the temperature, pressure, ...) is taken into account through the Q sampled random vectors $\tilde{\vec{y}}$.

The uncertainty propagation scheme can be applied regardless of the inversion routine being used, yet, the user must ensure that the chosen inversion algorithm does not bring additional uncertainty or, if it does, this new source of uncertainty, if not negligible, must be quantified and included in the uncertainty budget.

Next stage is to account for the modeling errors. Instead of a fixed model $\vec{\vec{H}}$, Q kernel matrices are randomly drawn. Drawing a random kernel matrix has the meaning of drawing the kernel matrix whose coefficients are computed with parameters (and functions) drawn from their respective random variables (and random processes).

However, among the sources of uncertainty, the time constants of the fluctuations vary and must be modeled in consequence. If the time constant of the source fluctuation is infinite, the source will not vary within a scan or between scans of the same experiment because it depends only on the device being used. When the time constant is in the order of magnitude of the scanning time of the experiment, the source is fixed for a given scan, and, it is updated between consecutive scans. On the contrary, if the time constant is shorter than the scanning time of the experiment, the source will vary within a scan[6] and between consecutive scans.

The flowchart shown in figure 4 summarizes the uncertainty propagation.

[6] A new sample is drawn for every channel (time interval of about 1 s).

Figure 4: Flowchart of the uncertainty propagation via the Monte Carlo method.

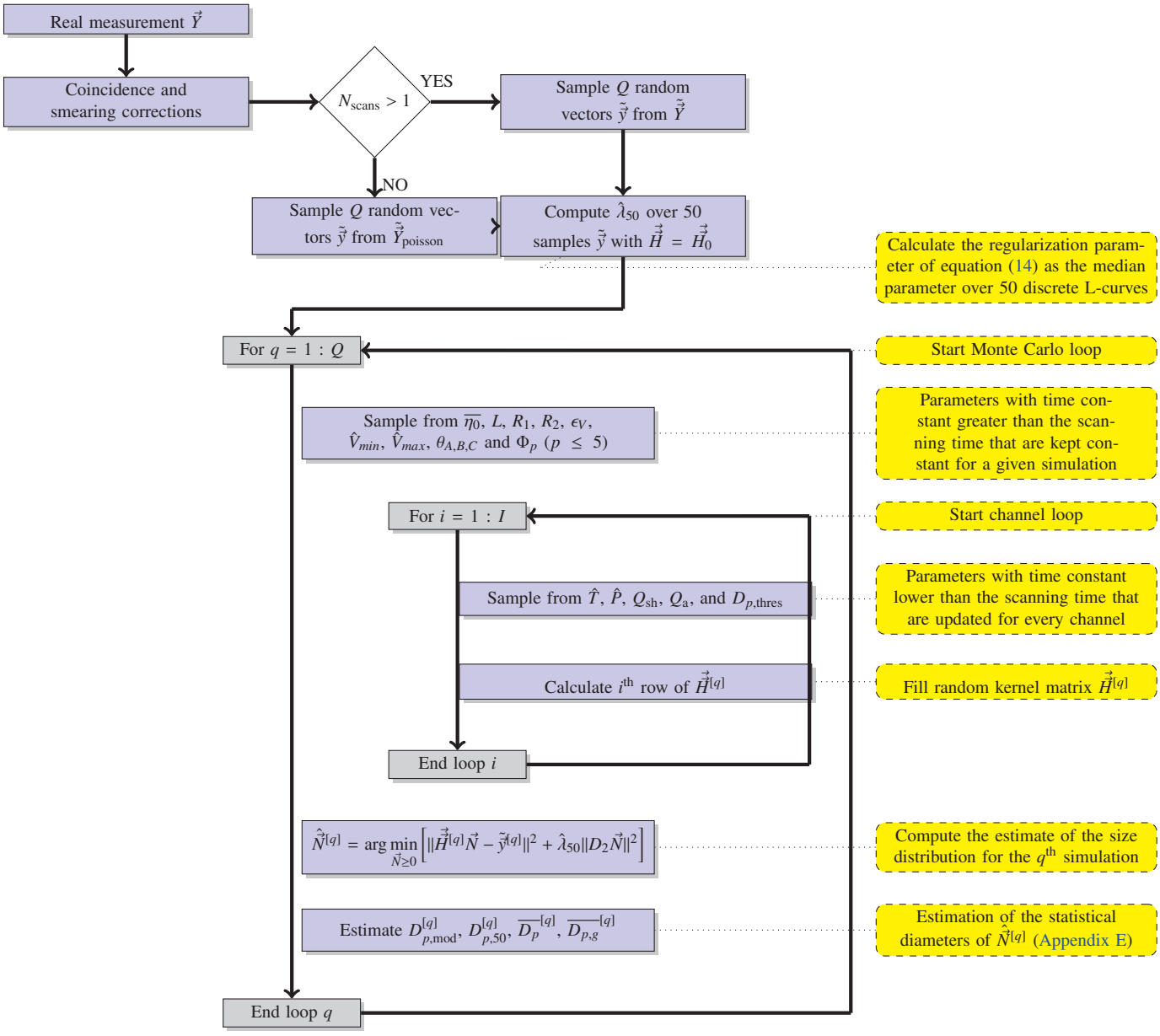

5. Results

In this section, the uncertainty propagation scheme is tested against real data sets. The particle samples under study are Standard Reference Materials. They are monosize polystyrene latex spheres (PSL) of different sizes: 100 nm, 200 nm and 450 nm. We conduct the experiments only for the 200 nm PSL. The 100 nm PSL and 450 nm PSL are TSI free data sets that one obtains when downloading AIM (Aerosol Instrument Manager) software. By choosing such data sets, we intend to check that the method is consistent, firstly with the commonly used approach, namely AIM software, and, secondly, with any kind of data, settings or devices being used.
Table 4 summarizes the settings for each data set. The output of the experiments is a number of particles counted over time.

Table 4: SMPS settings for the 100 nm PSL, 200 nm PSL and 450 nm PSL.

Parameters	**Variable**	**Unit**	**PSL 100 nm**	**PSL 200 nm**	**PSL 450 nm**
Classifier Model	-	-	TSI 46058	TSI 3080	TSI 3080
DMA Model	-	-	TSI 3081	TSI 3081	TSI 3081
Neutralizer Model	-	-	TSI 3088	TSI 3077	None
Detector Model	-	-	TSI 3772	TSI 3022	TSI 3025
Impactor	-	[cm]	None	0.0457	None
Ref Gas Viscosity	η_0	[kg/(m*s)]	1.832450×10^{-5}	1.832450×10^{-5}	1.820300×10^{-5}
Ref Mean Free Path	$\lambda_{m,0}$	[m]	6.73×10^{-8}	6.6420×10^{-8}	6.650×10^{-8}
Ref Gas Temperature	T_0	[K]	296.15	296.15	293.15
Ref Gas Pressure	P_0	[kPa]	101.30	101.30	101.3
Particle Density	ρ	[g/cc]	2.2	2.2	0.8
Temperature range	T	[K]	[295.65 - 296.15]	[292.75 - 293.15]	[293.15 - 293.15]
Pressure range	P	[kPa]	[98.20 - 98.20]	[101.0 - 101.1]	[101.3 - 101.3]
DMA Sheath Flow	q_{sh}	[lpm]	10.0	3.0	4.0
DMA Aerosol Flow	q_{a}	[lpm]	1.0	0.3	0.3
Detector Inlet Flow	q_{m}	[lpm]	1.0	0.3	0.3
Detector Sample Flow	q_{cpc}	[lpm]	1.0	0.3	0.03
Low Voltage range	V_{min}	[V]	[10.77 - 10.78]	[10.30 - 10.31]	[10.19 - 10.19]
High Voltage range	V_{max}	[V]	[9944.93 - 9949.66]	[9690.66 - 9699.31]	[9738.40 - 9738.40]
Scan Up Time	t_s	[s]	120	180	300
Retrace Time	t_r	[s]	6	30	15
Plumbing Time	t_d	[s]	1.03	3.53	3.38
Residence Time	t_f	[s]	2.26	7.52	5.77
DMA Inner Radius	r_1	[cm]	0.937	0.937	0.937
DMA Outer Radius	r_2	[cm]	1.961	1.961	1.961
DMA Length	L	[cm]	44.369	44.369	44.369
Number of scans	N_{scan}	-	3	15	2

First, care has to be taken in interpreting the results, indeed, as shown in the recent study of (Yang et al., 2018), particle stable charging cannot be achieved using TSI 3077 charger for the 200 nm PSL case. Nevertheless, the model used to represent the charging process is very conservative as depicted in figure 3. For that reason, the uncertainty propagated from the unstable charging is most likely already included in the current model. Figure 5 shows the measured particle count (every scan is plotted) as a function of the electrical mobility diameter D_p for PSL 100 nm (3 scans), 200 nm (15 scans) and 450 nm (2 scans). The 100 nm PSL reveals the presence of doubly charged monomers (around 70 nm), whereas the 200 nm PSL shows doubly charged monomers (around 140 nm) as well as dimers (around 260 nm). The 450 nm PSL is more difficult to analyze since the measured particle count is very low, yet, multiply charged monomers are

also suspected.

A MATLAB graphical user interface (GUI) has been developed in order to run the simulations. The amount of time taken to run a simulation is about one second. Figure 6 gives the results of the computations for each data set. The mean estimate of the PSD (red curve) and its 95% confidence region (grey shadow) are computed over $Q = 50000$ simulations. All results extracted from AIM software (1 curve per scan) are corrected for diffusion losses and multiply charged monomers. The results reveal that the estimates of the PSDs retrieved by AIM software and by the new approach are consistent in terms of peak concentration location and level of concentration. Moreover, for 200 nm PSL and 450 nm PSL, AIM estimates are in accordance with the computed 95% confidence region. It should be noted that AIM estimates are a bit broader at the peak location, especially for the 100 nm PSL.

From a more global perspective, the results suggest that the uncertainty can be kept reasonably low for very repeatable measurements as it is the case with the 100 nm PSL. Moreover, the particle concentration $dN/d\log(D_p)$ is far more subject to fluctuations than the particle mobility diameter D_p. For the 100 nm PSL, the particle count at $D_p \simeq 100$ nm varies between 220 and 270 particles and leads to a variation of $\pm 12\%$ of the peak concentration. For the 200 nm PSL, the particle count at $D_p \simeq 200$ nm varies between 250 and 375 particles and leads to a variation of $\pm 40\%$ of the peak concentration. As a consequence, given the largest measured fluctuation in the particle count, a simple rule of three yields to a first guess of the expected variation of the peak concentration. For the 200 nm PSL, this first guess would be $\pm 30\%$ and the remaining $\pm 10\%$ could be imputed to the other sources. Nevertheless such analysis cannot be extended to the 450 nm PSL that is a low concentration PSD. For these case, the shape of the confidence region reveals that both particle mobility diameter and concentration are subject to variations (distortion of the confidence region at the peak concentration). In fact, since the particle count follows a Poisson statistic, in such a low count situation, the peak location estimate varies between simulations.

If the confidence region is a widely used approach to provide the uncertainty associated with a 2-D function in the statistics field, the aerosol community generally expresses the size distribution in terms of statistical parameters (scalar representation) such as the mode diameter $D_{p,\mathrm{mod}}$, the median diameter $D_{p,50}$, the mean diameter $\overline{D_p}$, the geometric mean diameter $\overline{D_{p,g}}$ and the geometric standard deviation σ_g. These quantities are computed for every estimate of the size distribution $\hat{\vec{N}}$ (see Appendix E) and finally expressed in terms of expectation (average over the total number of simulations Q) and standard uncertainty (simply the standard deviation). Figure 7 offers a graphical comparison between the computed statistics available from AIM (repeatability analysis) with the new statistics brought by the new approach (full uncertainty analysis) and table 5 summarizes the numerical statistics computed by using the two methods. It gives an uncertainty comparison obtained from the proposed method and common repeatability. The measurement repeatability uncertainty is always smaller than that obtained from the full uncertainty analysis for the three cases studied here. As expected, accounting for modeling errors in the uncertainty propagation scheme enlarge

Table 5: Summary of the statistics for the 100 nm PSL, 200 nm PSL and 450 nm PSL.

	PSL 100 nm		**PSL 200 nm**		**PSL 450 nm**	
Statistics	Mean [nm]	St. Dev [nm]	Mean [nm]	St. Dev [nm]	Mean [nm]	St. Dev [nm]
Median	101.22	0.18	204.39	1.71	443.87	1.52
Mode	101.58	0.17	197.02	1.95	443.55	2.65
Geometric Mean	101.76	0.27	236.59	3.93	424.24	4.36
Mean	102.07	0.28	251.40	5.70	431.21	3.60
Median [AIM]	101.48	0.13	202.40	0.41	447.86	0.03
Mode [AIM]	101.45	0.00	196.09	0.26	446.32	0.27
Geometric Mean [AIM]	101.80	0.19	216.65	1.66	426.46	3.74
Mean [AIM]	102.13	0.21	222.17	1.51	433.98	2.91

the commonly reported uncertainty. The mean diameter and the geometric mean diameter are sensitive to fluctuations over the whole diameter range because they tend to measure a global behavior. For that reason, large differences exist between the computed diameters from AIM estimates and from the new approach especially for the 200 nm PSL. On the other hand, the mode diameter and the median diameter provide a central measure that is the reason why low differences appear.

Figure 5: Measured particle count as a function of the electrical mobility diameter for the 100 nm PSL (3 scans), 200 nm PSL (15 scans) and 450 nm PSL (2 scans).

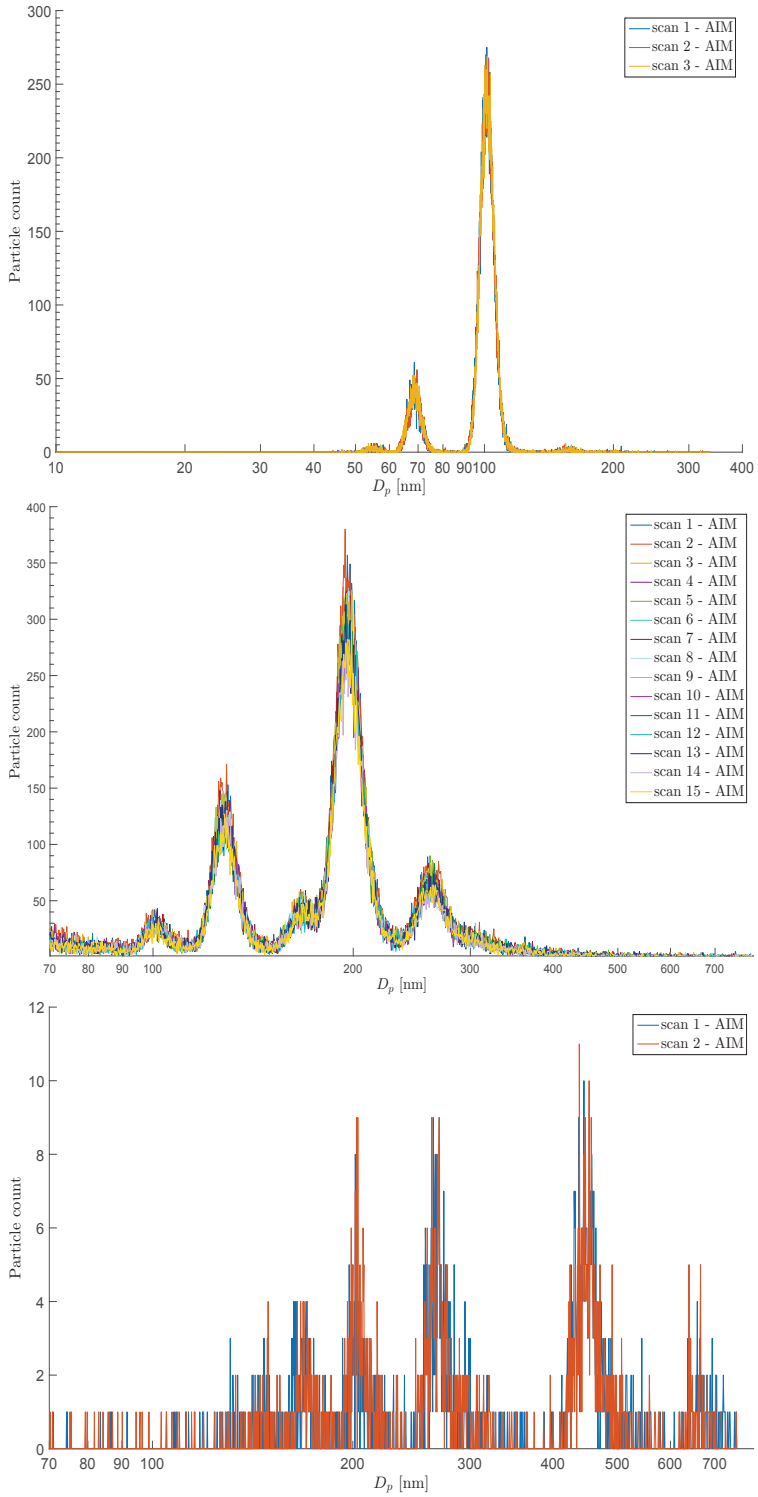

Figure 6: The mean estimate of the aerosol size distribution (red curve) over $Q = 50000$ simulations, its computed 95 % confidence region and AIM built-in software estimates (one estimate per scan) with multiple charge correction as well as diffusion losses correction for the 100 nm PSL , 200 nm PSL and 450 nm PSL.

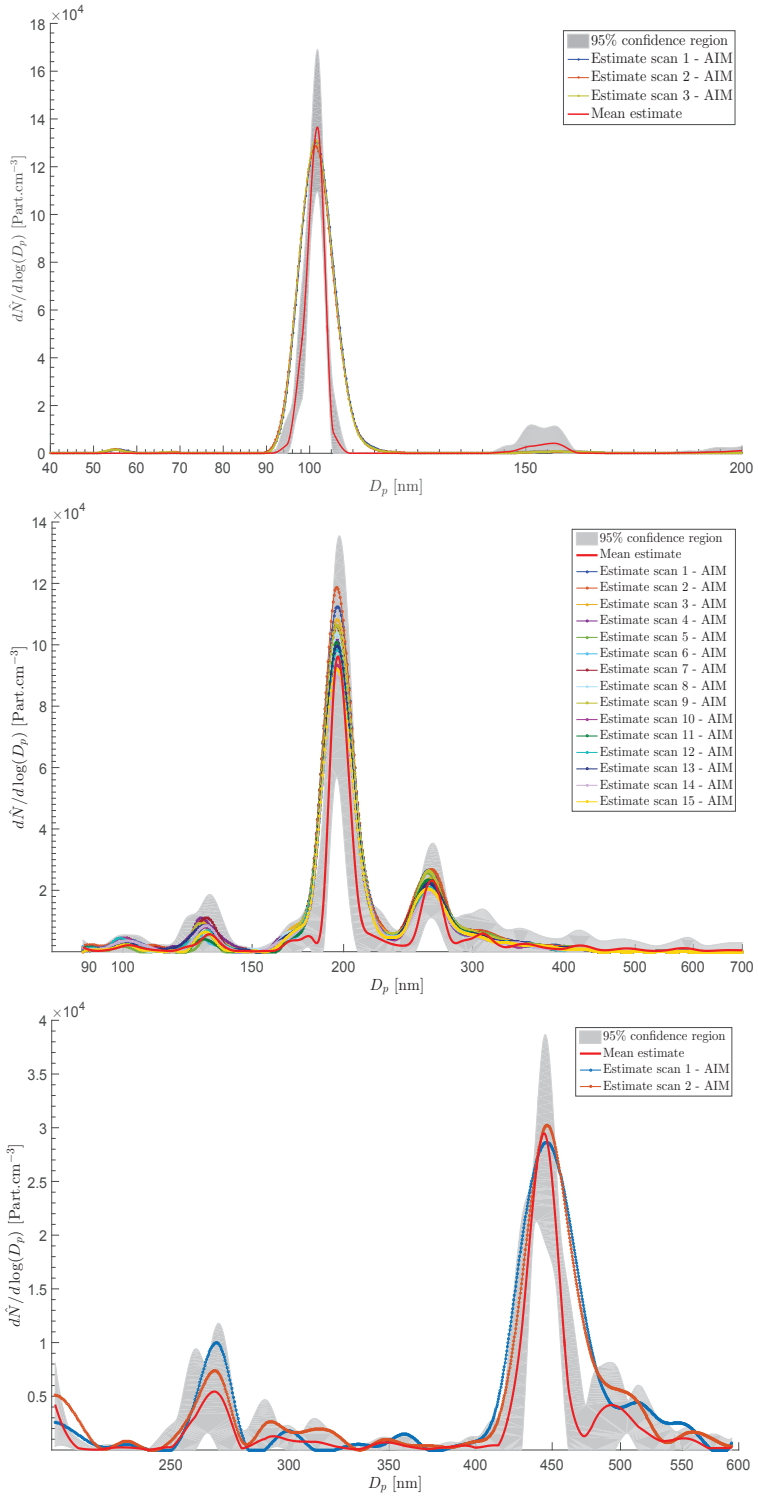

Figure 7: Comparison of the statistical diameters computed by using the new method (50000 simulations) for the 100 nm PSL, 200 nm PSL and 450 nm PSL with the experimental results obtained by AIM software. The red dots refer to the mean estimate and associated red bars refer to the standard deviation computed over the total number of simulations (full uncertainty analysis). The black dots refer to the average diameter computed over the number of real measurements and associated black bars represent the standard deviation (repeatability uncertainty).

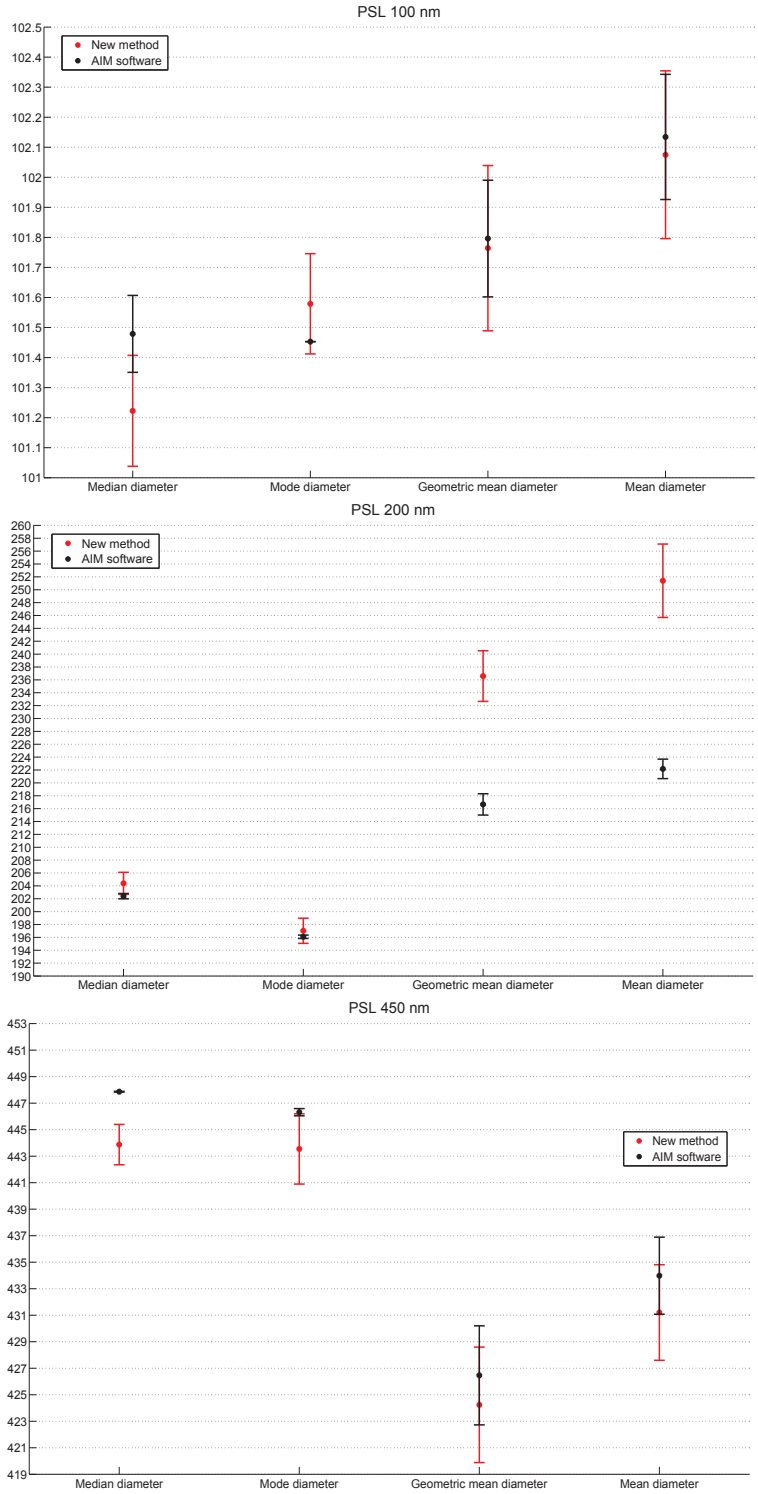

6. Conclusion

This paper brings the users with a new framework to perform uncertainty propagation computations for PSD measured with an SMPS by using the Monte Carlo method. The main effort was made with regard to investigating the very different existing approximations to model the physics. Innovative and consensual statistical models are shown that account for that many options to compute the bipolar charging law, the slip correction, the DMA transfer function, .. .

Since several quantities are still not measured during the day-to-day experiments, some of the statistical models may seem conservative to the readers. In fact, the proposed methodology will never be perfectly suited for every setup that is why, if more knowledge is available (new experiments, new publications, ...), we recommend to update the statistical model parameters (mean, variance, bounds, ...) or eventually create new ones.

The presented work reflects that the SMPS is well-designed for accurate sizing of airborne PSD with a very low uncertainty associated with the estimated particle mobility diameter (median particle sizes with relative standard uncertainty of ±0.17% for the 100 nm PSL, ±0.83% for the 200 nm PSL and ±0.34% for the 450 nm PSL). On the other hand, the peak particle number concentration uncertainty is very large and reaches ±40% for the 200 nm PSL and that is most likely due to the repeatability uncertainty (particle count measurement) and also to the conservative model set to represent the bipolar charging law. A fine characterization of the ionic population can considerably reduce the particle number concentration uncertainty by making such modeling more accurate.

Further work is still necessary to clearly identify the main contributors to uncertainty and to achieve a numerical evaluation of their respective contributions. A global sensitivity analysis is being investigated to solve this complex problem.

References

Allen, M. and Raabe, O. (1985), 'Slip correction measurements of spherical solid aerosol particles in an improved Millikan apparatus.', *Aerosol Science and Technology* **4**, 537–547.

Bartz, H., Fissan, H. and Liu, B. Y. H. (1987), 'A new generator for ultrafine aerosols below 10 nm', *Aerosol Science and Technology* **6**(2), 163–171.

Birge, R. T. (1945), 'Values of certain atomic constants with particular reference to the electronic charge', *American Journal of Physics* **13**, 63–73.

Biskos, G. (2004), 'Theoretical and experimental investigation of the differential mobility spectrometer'.

Chen, B. T., Schwegler-Berry, D., Cumpston, A., Cumpston, J., Friend, S., Stone, S. and Keane, M. (2016), 'Performance of a scanning mobility particle sizer in measuring diverse types of airborne nanoparticles: Multi-walled carbon nanotubes, welding fumes, and titanium dioxide spray', *Journal of occupational and environmental hygiene* **13**(7), 501–518.

Collins, D. R., Cocker, D. R., Flagan, R. C. and Seinfeld, J. H. (2004), 'The scanning DMA transfer function', *Aerosol Science and Technology* **38**(8), 833–850.

Collins, D. R., Flagan, R. C. and Seinfeld, J. H. (2002), 'Improved inversion of scanning DMA data', *Aerosol science and technology* **36**(1), 1–9.

Collins, M., Dick, W. and Romay, F. (2013), 'A new coincidence correction method for condensation particle counters', *Aerosol Science Technology* **47**(2), 177–182.

Dubey, P. and Dhaniyala, S. (2013), 'Improved inversion of scanning electrical mobility spectrometer data using a new multiscale expectation maximization algorithm', *Aerosol Science and Technology* **47**(1), 69–80.

Fuchs, N. A. (1963), 'On the stationary charge distribution of aerosol particles in a bipolar ionic atmosphere', *Geofisica Pura e Applicata* **56**(1), 185–193.

Fuchs, N. A. and Sutugin, G. A. (1970), *Highly Dispersed Aersols*, Ann Arbor Science.

Gormley, P. G. and Kennedy, M. (1949), 'Diffusion from a stream flowing through a cylindrical tube', *Proceedings of the Royal Irish Academy* **52A**, 163–169.

Hagwood, C., Sivathanu, Y. and Mulholland, G. (1999), 'The DMA transfer function with brownian motion a trajectory/monte-carlo approach', *Aerosol Science and Technology* **30**(1), 40–61.

Hansen, P. C., Jensen, T. K. and Rodriguez, G. (2007), 'An adaptive pruning algorithm for the discrete L-curve criterion', *Journal of Computational and Applied Mathematics* **198**(2), 483–492.

He, M. and Dhaniyala, S. (2014), 'Experimental characterization of flowrate-dependent bipolar diffusion charging efficiencies of sub-50 nm particles', *Journal of Aerosol Science* **76**(Supplement C), 175 – 187.
URL: *http://www.sciencedirect.com/science/article/pii/S0021850214001062*

Hoppel, W. and Frick, G. (1986), 'Ion aerosol attachment coefficients and the steady-state charge-distribution on aerosols in a bipolar ion environment', *Aerosol Science Technology* **5**(1), 1–21.

Hutchins, D., Harper, M. and Felder, R. (1995), 'Slip correction measurements for solid spherical particles by modulated dynamic light scattering.', *Aerosol Science and Technology* **22**, 202–218.

ISO 15900 (2009), 'Determination of particle size distribution-differential electrical mobility analysis for aerosol particles'.

ISO 27891 (2015), 'Aerosol particle number concentration calibration of condensation particle counters'.

JCGM 101 (2008), 'Evaluation of measurement data supplement 1 to the "guide to the expression of uncertainty in measurement" propagation of distributions using a Monte Carlo method'.

Jiang, J., Attoui, M., Heim, M., Brunelli, N. A., McMurry, P. H., Kasper, G., Flagan, R. C., Giapis, K. and Mouret, G. (2011), 'Transfer functions and penetrations of five differential mobility analyzers for sub-2 nm particle classification', *Aerosol Science and Technology* **45**(4), 480–492.

Jung, H., Mulholland, G. W., Pui, D. Y. H. and Kim, J. H. (2012), 'Re-evaluation of the slip correction parameter of certified PSL spheres using a nanometer differential mobility analyzer NDMA', *Journal of Aerosol Science* **51**, 24–34.

Kagi, N., Fujii, S., Horiba, Y., Namiki, N., Ohtani, Y., Emi, H., Tamura, H. and Kim, Y. S. (2007), 'Indoor air quality for chemical and ultrafine particle contaminants from printers', *Building and Environment* **42**(5), 1949 – 1954.
URL: *http://www.sciencedirect.com/science/article/pii/S0360132306000965*

Kim, J. H., Mulholland, G. W., Kukuck, S. R. and Pui, D. Y. H. (2005), 'Slip correction measurements of certified PSL nanoparticles using a nanometer differential mobility analyser Nano-DMA for knudsen number from 0.5 to 83', *Journal of Research of National Institute of Standards and Technology* **110**(1), 31–54.

Kinney, P., Pui, D., Mulholland, G. and Bryner, N. (1991), 'Use of the electrostatic classification method to 0.1 μm SRM particles - a feasibility study', *Journal of Research of the National Institute of Standards and Technology* **96**(2).

Knutson, E. O. and Whitby, K. T. (1975), 'Aerosol classification by electric mobility: Apparatus, theory, and applications', *Journal of Aerosol Science* **6**(6), 443–451.

Lawson, C. L. and Hanson, R. J. (1974), *Solving Least Squares Problems*, Prentice-Hall, Englewood Cliffs, NJ.

Mamakos, A., Ntziachristos, L. and Samaras, Z. (2007), 'Diffusion broadening of DMA transfer functions. numerical validation of stolzenburg model', *Journal of Aerosol Science* **38**(7), 747–763.

Markowski, G. R. (1987), 'Improving twomey's algorithm for inversion of aerosol measurement data', *Aerosol Science and Technology* **7**(2), 127–141.

Mathis, U., Ristimki, J., Mohr, M., Keskinen, J., Ntziachristos, L., Samaras, Z. and Mikkanen, P. (2004), 'Sampling conditions for the measurement of nucleation mode particles in the exhaust of a diesel vehicle', *Aerosol Science and Technology* **38**(12), 1149–1160.

Motzkus, C., Macé, T., Gaie-Levrel, F., Ducourtieux, S., Delvallee, A., Dirscherl, K., Hodoroaba, V.-D., Popov, I., Popov, O., Kuselman, I., Takahata, K., Ehara, K., Ausset, P., Maillé, M., Michielsen, N., Bondiguel, S., Gensdarmes, F., Morawska, L., Johnson, G. R., Faghihi, E. M., Kim, C. S., Kim, Y. H., Chu, M. C., Guardado, J. A., Salas, A., Capannelli, G., Costa, C., Bostrom, T., Jämting, Å. K., Lawn, M. A., Adlem, L. and Vaslin-Reimann, S. (2013), 'Size characterization of airborne SiO_2 nanoparticles with on-line and off-line measurement techniques: an interlaboratory comparison study', *Journal of Nanoparticle Research* **15**(10), 1919.

Mulholland, G., Donnelly, M., Hagwood, C., Kukuck, S., Hackley, V. and Pui, D. (2006), 'Measurement of 100 nm and 60 nm particle standards by differential mobility analysis', *Journal of Research of the National Institute of Standards and Technology* **111**(4), 257.

Niida, T., Wen, H., Udischas, R. and Kasper, G. (1988), 'Counting efficiency of condensation nuclei counters in N_2, Ar, CO_2 and He', *Aerosol Science and Technology* **19**(7), 1417–1420.

Oberdörster, G., Sharp, Z., Atudorei, V., Elder, A., Gelein, R., Kreyling, W. and Cox, C. (2004), 'Translocation of inhaled ultrafine particles to the brain', *Inhalation Toxicology* **16**(6-7), 437–445.

Park, J., Sakurai, H., Vollmers, K. and McMurry, P. H. (2004), 'Aerosol size distributions measured at the south pole during {ISCAT}', *Atmospheric Environment* **38**(32), 5493 – 5500. Antarctic Atmospheric Chemistry: {ISCAT} 2000.
URL: *http://www.sciencedirect.com/science/article/pii/S135223100400528X*

Phillips, D. (1962), 'A technique for the numerical solution of certain integral equations of the first kind', *Journal of the Association for Computing Machinery* **9**(1), 84–97.

Ravenzwaay, B. V., Landsiedel, R., Fabian, E., Burkhardt, S., Strauss, V. and Ma-Hock, L. (2009), 'Comparing fate and effects of three particles of different surface properties: Nano-tio2, pigmentary tio2 and quartz', *Toxicology Letters* **186**(3), 152 – 159. Toxicity of Engineered Nanomaterials.

Reischl, G. P., Mkel, J. M., Karch, R. and Necid, J. (1996), 'Bipolar charging of ultrafine particles in the size range below 10 nm', *Journal of Aerosol Science* **27**(6), 931–949.
URL: *http://www.sciencedirect.com/science/article/pii/0021850296000262*

Russell, L. M., Flagan, R. C. and Seinfeld, J. H. (1995), 'Asymmetric instrument response resulting from mixing effects in accelerated DMA-CPC measurements', *Aerosol Science and Technology* **23**, 491–509.

Scheibel, H. and Porstendörfer, J. (1983), 'Generation of monodisperse Ag- and NaCl-aerosols with particle diameters between 2 and 300 nm', *Journal of Aerosol Science* **14**(2), 113 – 126.

Seinfeld, J. H. and Wolfenbarger, J. K. (1990), 'Inversion aerosol size distribution data', *Journal of Aerosol Science* **21**(2), 227–247.

Sem, G. J. (2002), 'Design and performance characteristics of three continuous-flow condensation particle counters: a summary', *Atmospheric Research* **62**(34), 267 – 294.

Stolzenburg, M. R. (1988), An Ultrafine Aerosol Size Distribution Measuring System, PhD thesis, University of Minnesota, Minneapolis.

Talukdar, S. S. and Swihart, M. T. (2003), 'An improved data inversion program for obtaining aerosol size distributions from scanning differential mobility analyzer data', *Aerosol Science and Technology* **37**, 145–161.

Twomey, S. (1963), 'On the numerical solution of fredholm integral equations of the first kind by the inversion of the linear system produced by quadrature', *Journal of the Association for Computing Machinery* **10**, 97–101.

Twomey, S. (1975), 'Comparison of constrained linear inversion and an iterative non-linear algorithm applied to the indirect estimation of particle size distributions', *Journal of Computational Physics* **18**, 188–200.

Vogt, R., Scheer, V., Casati, R. and Benter, T. (2003), 'On-road measurement of particle emission in the exhaust plume of a diesel passenger car', *Environmental Science and Technology* **37**(18), 4070–4076.

Voutilainen, A. (2001), 'Statistical inversion methods for the reconstruction of aerosol size distributions', *Report series in aerosol science* pp. 188–200.

Wahba, G. (1977), 'Practical approximate solutions to linear operator equations when the data are noisy', *SIAM Journal on Numerical Analysis* **14**(4), 651–667.

Wang, S. C. and Flagan, R. C. (1990), 'Scanning electrical mobility spectrometer', *Aerosol Science and Technology* **13**(2), 230–240.

Wiedensohler, A. (1988), 'An approximation of the bipolar charge distribution for particles in the submicron size range', *Journal of Aerosol Science* **19**(3), 387–389.

Yang, H., Dhaniyala, S. and He, M. (2018), 'Performance of bipolar diffusion chargers: Experiments with particles in the size

range of 100 to 900 nm', *Aerosol Science and Technology* **52**(2), 182–191.
URL: *https://doi.org/10.1080/02786826.2017.1387641*

Appendix A. Sources of uncertainty

Appendix A.1. Coincidence correction

Coincidence occurs when more than one particle occupies the optical sensing region simultaneously. Coincidence theory describes the deviation and non linearity between true and observed counting rate for high concentrations of particles. (Collins et al., 2013) derived an expression to calculate the true rate of coincidence using the Lambert W function. The actual particle count, denoted as $\vec{Y}_a$, is a function of the measured particle count, $\vec{Y}$, and of the CPC per-event dead time, τ_{cpc}, via the following equation

$$\vec{Y}_a = \frac{-W(-\vec{Y}\tau_{cpc})}{\tau_{cpc}}. \tag{A.1}$$

Please note that CPCs recent models already correct for coincidence and one must first check whether this treatment is already done on the data.
The measured particle count are corrected for coincidence and no additional uncertainty has been introduced for it (fixed correction).

Appendix A.2. Smearing effect correction

The plumbing delay is the time a classified particle must travel after exiting the DMA until it is detected by the CPC. Due to mixing and deviations from plug flow within the tubing and the CPC, the particles experience several delay times. (Russell et al., 1995) examined the smearing of the transfer function as a result of flow disturbances in the system and developed a model to predict the distortion of the transfer function in terms of the delay time distribution. Nevertheless, they did not incorporate the diffusional broadening of the DMA transfer function into their derivation. Later, (Collins et al., 2002) have developed a simplified approach with an adjustment of the raw data to account for the delay time distribution prior to the final inversion. Their method is preferred here.

Appendix A.3. Temperature, Pressure

Gas temperature and pressure, T and P, must be controlled for an accurate sheath flow rate q_{sh}. Indeed, SMPS uses thermal flow sensors that are sensitive to changes in air density and air velocity which is the reason why such flowmeters indicate flow rate with reference to a set of standard conditions in terms of temperature and pressure.

Statistical Modeling. For a given two minutes scan, SMPS embedded software prints out a unique couple for the gas temperature and pressure (T, P). Given that the gas temperature and pressure are not measured during the experiment and that both quantities have time constants lower than the scan duration, additional assumptions are necessary. As a first approximation, we consider to set tolerances on both quantities. T is modeled as a sample drawn from a uniform random variable $\hat{T}$ with $\hat{T} \sim \mathcal{U}(T - \Delta T, T + \Delta T)$ and $\Delta T = 0.5°$ C. P is modeled as a sample drawn from a uniform random variable $\hat{P}$ with $\hat{P} \sim \mathcal{U}(P - \Delta P, P + \Delta P)$ and $\Delta P = 100$ Pa.
New samples will be drawn from their respective distributions, namely $\hat{T}$ and $\hat{P}$, for every time of the simulation following the argument of time constants shorter than the scanning time. When several scans are available, T and P will be replaced by the average gas temperature and gas pressure over the number of scans. In such situation, ΔT and ΔP shall be re-adjusted.

Appendix A.4. Viscosity of air (Mulholland et al., 2006)

The viscosity of air η_0 is used to compute the dynamic gas viscosity η_g that will be used to determine the particle electrical mobility Z_d. (Birge, 1945) reported the weighted average value of the viscosity of air, $\eta_0 = (1.83245 \pm 0.00069) \times 10^{-5}$ kg.m^{-1}.s^{-1} from six different results. For a new temperature T, the viscosity η_g can be obtained using the Sutherland formula

$$\eta_g = \eta_0 \times \left(\frac{T}{T_0}\right)^{3/2} \times \left(\frac{T_0 + S}{T + S}\right), \tag{A.2}$$

Statistical Modeling. The viscosity of air is modeled as a sample drawn from the normal random variable $\overline{\eta_0}$ with $\overline{\eta_0} \sim \mathcal{N}(\eta_0, \sigma^2_{\eta_0})$ and $\sigma_{\eta_0} = 0.00069 \times 10^{-5}$ kg.m^{-1}.s^{-1}.

Appendix A.5. Geometric factors

The geometry of the DMA defines the air flow field inside the classification region, the electric field and the trajectory of the particle inside the column. (Kinney et al., 1991) have computed the uncertainty associated with the values of the center rod radius r_1 (±0.2%), the outer cylinder radius r_2 (±0.3%) and the length of the DMA column l (±0.5%) for the electrostatic classifier TSI Model 3071 (Long DMA). For the nano-DMA mainly used to size ultra-fine aerosol particles, only a tolerance is associated with each dimension.

Statistical Modeling. The manufacturer states that the tolerances represent the greatest deviations possible. From such information, l, r_1 and r_2 are modeled as samples drawn from uniform random variables L, R_1 and R_2 whose bounds are taken as the given tolerances.

Appendix A.6. DMA flow rates

The sheath flow rate q_{sh} is directly linked to the electrical mobility (see equation (1)), so any fluctuations of q_{sh} result in broadening the transfer function of the DMA. SMPS utilizes a recirculating flow scheme so that q_{sh} matches the exhaust flow q_{ex}. Such scheme secures equality of q_{sh} and q_{ex} within 0.01% ((Mulholland et al., 2006)). This is why the leakage rate in the recirculation system has not been investigated here. The DMA controller ensures a laminar flow in order to minimize the flow disturbances that cause decreasing resolution, it also ensures balanced flows ($q_a = q_m$). The internal flow-meters which control the sheath and bypass flow are NIST traceable, micro-processor controlled, and they adjust for differences of temperature T and pressure P. The flow-meter uncertainty is stated measuring dry gas (less than 10 % Relative Humidity) at standard conditions of 21.1°C and 101.3 kPa. The computed uncertainty accounts for the reading repeatability, the resolution (display) and the correction due to the calculations to retrieve the volumetric flow rate[7] from the measured standard flow rate[8].

The sheath flow rate was measured by a flow-meter Model 4140 manufactured by TSI Incorporated during 1000 s (more than 15 minutes) for 3 set-point values: 3 lpm, 6 lpm and 10 lpm. The flow rate is recorded with a sampling rate of 1 Hz.

Table A.6 gives some descriptive statistics (min value, 1st and 3rd quartiles, median, mean, standard deviation and %RSD) for the measured sheath air flow for every set-point value. The results reflect a well-controlled sheath flow rate with very small dispersion around the setpoint value.

The percent relative standard deviations (%RSD) are 0.28% for 3 lpm, 0.41% for 6 lpm and 0.35% for 10 lpm. The flow-meter reading uncertainty varies between 0.005 and 0.010 lpm, depending on the measured

[7]The volumetric flow rate is the true volume flow of the gas exiting the flow-meter.

[8]The standard flow rate is the flow rate the air would be moving if T and P were at 21.1°C and 101.3 kPa.

Table A.6: Statistics summary for the sheath flow rate monitoring experiment.

Setpoint values \ Statistics	min	1st quartile	median	mean	3rd quartile	max	standard deviation	%RSD
3 lpm	2.97	3.00	3.00	3.00	3.00	3.03	0.01	0.28
6 lpm	5.90	5.99	6.00	6.00	6.00	6.13	0.02	0.41
10 lpm	9.86	9.98	9.99	9.99	10.01	10.14	0.03	0.35

gas and its resolution varies between 0.001 and 0.010 lpm depending on the flow rate measurement range (0.001 lpm when the flow rate is less than 9 lpm and 0.01 lpm otherwise). On the basis of this short analysis, the total %RSD is no more than 1%. Standard (ISO 15900, 2009) gives a sheath air flow standard uncertainty of ±0.06 lpm when q_{sh} is set to 3 lpm which corresponds to a relative standard uncertainty of 2%.

Statistical Modeling. The sampled flow rates are normally distributed for low flow rates and tend to follow a t-distribution for higher flow rates since larger tails are observed. To simplify the process, the sheath air flow rate is sampled from a Gaussian random variable Q_{sh} such that $Q_{sh} \sim \mathcal{N}(q_{sh_0}, \sigma_{q_{sh}})$, q_{sh_0} being the set-point value and $\sigma_{q_{sh}} = 0.02 \times q_{sh_0}$. We decide to apply the relative standard uncertainty of 2% for any q_{sh_0}: for $q_{sh_0} = 6$ lpm, the standard uncertainty is 0.12 lpm and for $q_{sh_0} = 10$ lpm, it is 0.2 lpm. Such modeling seems appropriate since these estimates are consistent with the experimental results presented in table A.6. As no leakage is assumed as well as balanced flows, the other flow rates (mean value and standard deviation) are directly deduced from Q_{sh}: $Q_{sh} = Q_{ex}$, $Q_a = Q_{sh}/10$ [9] and $Q_m = Q_a$.

Appendix A.7. Diffusion losses

When particles are smaller than 100 nm, Brownian motion creates a net flux of particles from regions with high concentrations towards regions with low concentrations. The walls of a tube are a sink for small particles creating a region of low concentration near them. This is why diffusion always generates a net transport of particles to the walls where they deposit. This mechanism affects the measured particle count and, as a consequence, the estimated PSD will under represent small particles.
Diffusion losses in the SMPS are frequently characterized in terms of penetration efficiencies. To compute the total penetration through the system, η, five different flow paths are distinguished:

- the penetration through the impactor inlet, η_{inlet},
- the penetration through the neutralizer and internal plumbing, $\eta_{neutralizer}$,
- the penetration through the tubing to the DMA and CPC, η_{tube},
- the penetration through the DMA, η_{DMA},
- the penetration through the CPC, η_{CPC}.

The DMA transfer function and the CPC detection efficiency that will be presented later in section 3.12 and 3.13 stand for the penetration through the DMA and through the CPC, respectively.
The penetration efficiency through the tubing, η_{tube}, is computed based on the (Gormley and Kennedy, 1949) equation:

[9] 10 corresponds to an aerosol-to-sheath ratio of 0.1. This value must be updated if the ratio changes.

$$\eta_{\text{tube}} = 0.819\exp(-14.63\Delta) + 0.0976\exp(-89.22\Delta) + 0.0325\exp(-228\Delta), \tag{A.3}$$

where Δ is the diffusion parameter for a circular tube

$$\Delta = \frac{DL_{\text{tube}}}{4\bar{v}R_{\text{tube}}^2}, \tag{A.4}$$

R_{tube} and L_{tube} being respectively the tube radius and length, $\bar{v}$ the mean velocity in the tube and D the diffusion coefficient related to D_p via the Stokes-Einstein relation

$$D = \frac{k_b T C_c(D_p)}{3\pi\eta_g D_p}. \tag{A.5}$$

The penetration efficiency through the impactor inlet, η_{inlet} is computed based on the (Gormley and Kennedy, 1949) modified equation using an effective length:

$$\eta_{\text{inlet}} = 0.82\exp(-11.5\mu) + 0.10\exp(-70.0\mu) + 0.03\exp(-180\mu) + 0.02\exp(-340\mu), \tag{A.6}$$

where $\mu = (DL_{\text{eff}})/q_m$, q_m being the sampling flow rate and L_{eff} the effective tube length. The penetration efficiency through the neutralizer and internal plumbing, $\eta_{\text{neutralizer}}$, is computed in a similar fashion with a different value of L_{eff}.

Statistical Modeling. The total penetration efficiency η is simply the product of the individual efficiencies,

$$\eta = \eta_{\text{inlet}} \times \eta_{\text{neutralizer}} \times \eta_{\text{tube}} \times \eta_{\text{DMA}} \times \eta_{\text{CPC}}, \tag{A.7}$$

where η is a function of the particle diffusion coefficient D, effective length L_{eff} and flow rate q_m. Obviously, the effective lengths vary among SMPSs and shall be adjusted depending on the device in use (for instance, $L_{\text{eff}} = 0.4$ m (He and Dhaniyala, 2014) in the calculations of $\eta_{\text{neutralizer}}$ for the Model TSI 3077 Neutralizer and $L_{\text{eff}} = 0.57$ m in the calculations of η_{inlet} for an inertial impactor size of 0.0457 cm). Then, they will be considered as fixed and no additional uncertainty will be introduced for it. . The uncertainty in the total penetration efficiency directly comes from D and q_m. As a reminder, D is a function of the slip correction, the gas temperature T and the dynamic gas viscosity η_g that are all uncertain quantities as described in previous sections.

Appendix B. Dynamic voltage measurement

Appendix B.1. Experimental results

A high voltage calibration facility was set up to measure the voltage of the DMA rod using a high voltage divider and a digital voltmeter in a similar fashion as what was done in (Mulholland et al., 2006). The output signal was measured using a Hewlett Packard 3458A digital multimeter. 2 configurations have been studied where only the scanning time t_s varies: 120 s and 180 s. 8 measurements are recorded for every configuration with a 10 Hz sampling rate.

Figure B.8 shows the standard relative voltage uncertainty (repeatability uncertainty) in percent as a function of the voltage for the two scanning times. The results reveal a high level of repeatability of the voltage ramp. Indeed, the relative voltage uncertainty is almost constant over the range of voltages being measured for $t_s = 120$ s and $t_s = 180$ s with their maximum values close to 1.5 % and 1 %, respectively. For this reason, we recommend to lengthen the scanning time in order to ensure a slowly-varying voltage ramp.

Appendix B.2. Model versus measurement

Since the voltage is not measured during the day-to-day measurements, a validation step is required for ensuring the adequacy between voltage ramp model and experimental results. SMPS embedded software provides the users with the estimates of $V_{\min}^{AIM}$ and $V_{\max}^{AIM}$ for every scan.

Let V^i the voltage ramp calculated according to equation (6) with the estimates $V_{\min}^{AIM,i}$ and $V_{\max}^{AIM,i}$ for scan i and $V_{\exp}^{i}$ the measured voltage for scan i. The mean voltage offset (or mean bias), denoted $\overline{\delta}_V$, is given by $\overline{\delta}_V[t] = \frac{1}{8}\sum_{i=1}^{8}\left(V_{\exp}^{i}(t) - V^i(t)\right)$.

Figure B.9 shows the computed mean voltage bias for the two scanning times. The offsets are not centered around zero as would be expected for an unbiased model. Still, the maximum offset value is about ±20 V within the time range.

Figure B.8: Voltage relative uncertainty $\left(\frac{\sigma(V)}{\overline{V}}\right)$ in percent as a function of the voltage for the two scanning times: 120 s and 180 s.

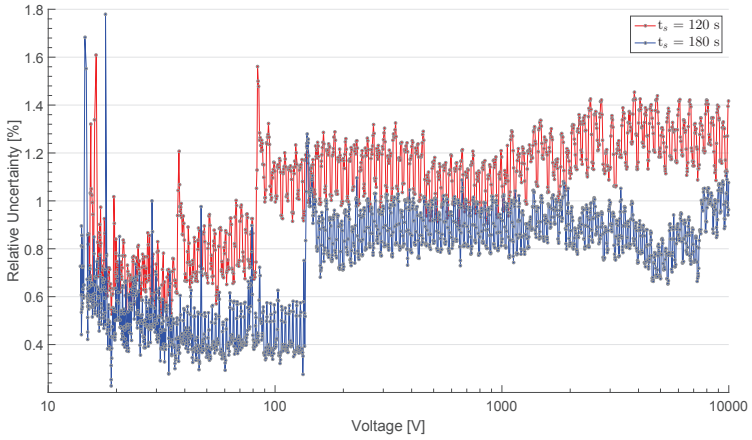

Figure B.9: Voltage mean bias $\overline{\delta}$ as a function of the voltage for the two scanning times: 120 s and 180 s.

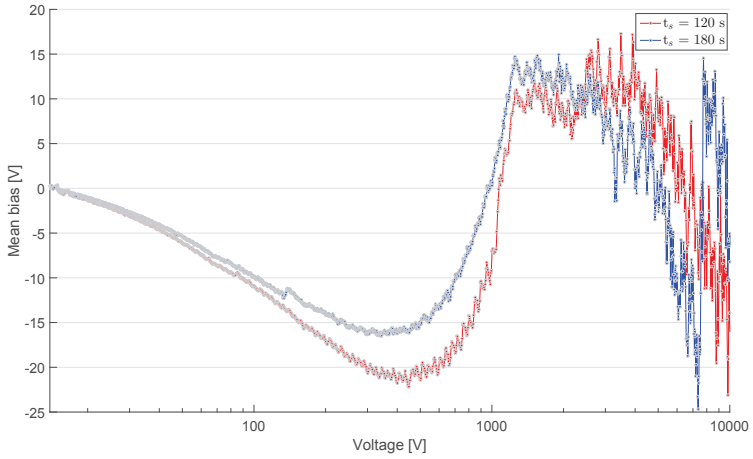

Appendix C. Calculations of the combination coefficient of positive and negative ions with a particle carrying *p* elementary units of charge by (Fuchs, 1963)

The combination coefficient $\beta_p^{\pm}$ of positive and negative ions with a particle carrying p elementary units of charge (p is considered positive, if the charges of the ion and the particle are of the same sign) can be written as:

$$\beta_p^{\pm} = \frac{\pi v_I^{\pm} \alpha_p^{\pm} \delta_I^{\pm 2} \exp\left(-\frac{\varsigma_p(\delta_I^{\pm})}{k_b T}\right)}{1 + \exp\left(-\frac{\varsigma_p(\delta_I^{\pm})}{k_b T}\right) \frac{v_I^{\pm} \alpha_p^{\pm} \delta_I^{\pm 2}}{4 D_I^{\pm} R_p} \int_0^{\frac{R_p}{\delta_I^{\pm}}} \exp\left(\frac{\varsigma_p\left(\frac{R_p}{\xi}\right)}{k_b T}\right) d\xi}, \tag{C.1}$$

where $\alpha_p^{\pm}$ is the probability of an ion (positive or negative) entering the limiting-sphere to collide and transfer its charge to the particle (collision probability), δ_I is the limiting sphere radius and ς_p is the electrostatic potential energy of an ion in the field of the particle given as:

$$\varsigma_p(r) = \int_r^{+\infty} F_{\text{int}} dr = \frac{1}{4\pi\epsilon_0}\left(\frac{pe^2}{r} - \kappa \frac{R_p^3}{2r^2(r^2 - R_p^2)}\right), \quad \kappa = \frac{(\epsilon_1 - 1)e^2}{\epsilon_1 + 1}, \tag{C.2}$$

where F_{int} is the force of electrostatic interaction between the ion and the particle, r is the distance of the ion from the center of the particle and κ is the image force parameter for particles with dielectric constant ϵ_1. The radius of the limiting sphere δ_I is given as follows:

$$\delta_I^{\pm} = \frac{R_p^3}{\lambda_I^{\pm 2}}\left(\frac{1}{5}\left(1 + \frac{\lambda_I^{\pm}}{R_p}\right)^5 - \frac{1}{3}\left(1 + \frac{\lambda_I^{\pm 2}}{R_p^2}\right)\left(1 + \frac{\lambda_I^{\pm}}{R_p}\right)^3 + \frac{2}{15}\left(1 + \frac{\lambda_I^{\pm}}{R_p}\right)^{\frac{5}{2}}\right). \tag{C.3}$$

In the absence of electrical forces, $\alpha_p^{\pm}$ is given as the square of the ratio of the particle radius to the limiting sphere:

$$\alpha_p^{\pm} = \left(\frac{R_p}{\delta_I^{\pm}}\right)^2. \tag{C.4}$$

For the case of charged particles, $\alpha_p^{\pm}$ is calculated according to the impact parameter b of the minimum apsoidal distance, denoted as $b_{\min}$:

$$\alpha_p^{\pm} = \left(\frac{b_{\min}}{\delta_I^{\pm}}\right)^2. \tag{C.5}$$

The equation that relates the impact parameter b to the apsoidal distance r_a comes from the two-body theory of classical mechanics, so $b_{\min}$ is computed as the minimum of

$$b^2 = r_a^2\left(1 + \frac{2}{3k_bT}\left(\varsigma_p(\delta_I) - \varsigma_p(r_a)\right)\right). \tag{C.6}$$

At this stage, 4 ionic properties are required to compute the ion-aerosol attachment coefficients $\beta_p^{\pm}$: the electrical mobilities and the masses of small ions (positive and negative), denoted as $z_I^{\pm}$ and $m_I^{\pm}$. Indeed, the diffusion $D_I^{\pm}$, the ionic mean thermal velocity $v_I^{\pm}$ and the mean free path of small ions $\lambda_I^{\pm}$ are deduced from them with the following relations:

$$D_I^{\pm} = \frac{k_bTz_I^{\pm}}{e}, \quad v_I^{\pm} = \sqrt{\frac{8k_bT}{\pi m_I^{\pm}}}, \quad \lambda_I^{\pm} = \frac{16\sqrt{2}}{3\pi}\frac{D_I^{\pm}}{v_I^{\pm}}\left(\frac{M}{M+m_I^{\pm}}\right)^{\frac{1}{2}}. \tag{C.7}$$

The expression for the mean free path of small ions is taken from (Fuchs and Sutugin, 1970) following the argument of consistency of (Reischl et al., 1996).

Appendix D. DMA transfer functions: ideal and diffusive

Appendix D.1. Non-diffusive transfer function

(Knutson and Whitby, 1975) developed DMA theory based on particle trajectory equations for a fixed voltage V. Neglecting particle diffusivity and assuming that the electric field is ramped exponentially with time, (Wang and Flagan, 1990) derived the expression of the non-diffusive transfer function ω_{nd} for a scanning DMA

$$\omega_{\text{nd}}(D_p, p, t) = \max\left[0, \min\left(\frac{s(D_p,p,t) + q_{\text{m}} - q_{\text{sh}}}{q_{\text{a}}}, \frac{-s(D_p,p,t) + q_{\text{a}} + q_{\text{sh}}}{q_{\text{a}}}, \frac{q_{\text{m}}}{q_{\text{a}}}, 1\right)\right], \tag{D.1}$$

where s is the so called mobility parameter that is computed for particles that reach the sample extraction slot at time $t - t_d$ and it is given by the following expression

$$s(D_p, p, t) = 2\pi r_1 Z_d(p, D_p) l \frac{V_{\min}\tau_v}{t_f}\left(1 - \exp\left(\frac{-t_f}{\tau_v}\right)\right)\exp\left(\frac{t - t_d}{\tau_v}\right). \tag{D.2}$$

Later, (Collins et al., 2004) have simulated ω for a long DMA (TSI Model 3081). They exhibit distortions in that configuration and brought simplified corrections to adjust the concentration and mobility of size distributions recovered with fixed voltage transfer function. Their corrections only apply for an aerosol to sheath flow ratio of 0.1.

Appendix D.2. Diffusive transfer function

The most widely used approach that includes particle diffusivity on the transfer function of the DMA is that of (Stolzenburg, 1988). He convoluted the non-diffusive transfer function with a Gaussian distribution to model the diffusive deviations of the particles along their ideal trajectories. Its expression can be modified, replacing the fixed voltage V by $\overline{V(t)}$ (cf equation (7)), such that ω_d can be written as follows

$$\omega_\mathrm{d}(D_p,p,t)=\frac{\tilde{\sigma}}{\sqrt{2}\beta(1-\delta)}\left[\epsilon_\omega\left(\frac{\frac{Z_d(p,D_p)}{Z^*(\overline{V(t)})}-(1+\beta)}{\sqrt{2}\tilde{\sigma}(p,D_p,t)}\right)+\epsilon_\omega\left(\frac{\frac{Z_d(p,D_p)}{Z^*(\overline{V(t)})}-(1-\beta)}{\sqrt{2}\tilde{\sigma}(p,D_p,t)}\right)-\epsilon_\omega\left(\frac{\frac{Z_d(p,D_p)}{Z^*(\overline{V(t)})}-(1+\beta\delta)}{\sqrt{2}\tilde{\sigma}(p,D_p,t)}\right)-\epsilon_\omega\left(\frac{\frac{Z_d(p,D_p)}{Z^*(\overline{V(t)})}-(1-\beta\delta)}{\sqrt{2}\tilde{\sigma}(p,D_p,t)}\right)\right], \tag{D.3}$$

The dimensionless flow parameters β and δ in equation (D.3) are defined as

$$\beta=\frac{q_\mathrm{a}+q_\mathrm{m}}{q_\mathrm{sh}+q_\mathrm{ex}},\qquad \delta=\frac{q_\mathrm{m}-q_\mathrm{a}}{q_\mathrm{m}+q_\mathrm{a}}, \tag{D.4}$$

and the function ϵ_ω is given by

$$\epsilon_\omega(x)=\int_0^x \mathrm{erf}(u)du = x\,\mathrm{erf}(x)+\frac{\exp(-x^2)}{\sqrt{\pi}}. \tag{D.5}$$

Stolzenburg derived the expression of the diffusive motion of particles inside the column of the classifier, denoted $\tilde{\sigma}$, where

$$\tilde{\sigma}(p,D_p,t)=\sqrt{G\frac{Z_d(p,D_p)}{Z^*(\overline{V(t)})}\ln\left(\frac{r_2}{r_1}\right)\frac{k_bT}{peZ^*(\overline{V(t)})}}, \tag{D.6}$$

and it depends on the geometric parameter G

$$G=\frac{4(1+\beta)^2}{1-\frac{r_1^2}{r_2^2}}\left[I\left(\frac{r_1^2}{r_2^2}\right)+\left(\frac{r_2^2-r_1^2}{2(1+\beta)lr_2}\right)^2\right], \tag{D.7}$$

and on the function I that was derived for plug flow (I_plug) and for fully developed flow (I_fulldev)

$$I_\mathrm{plug}(x)=\frac{1+x}{2},\qquad I_\mathrm{fulldev}(x)=\frac{\frac{1}{4}(1-x^2)(1-x)^2+\frac{5}{18}(1-x^3)(1-x)\ln(x)+\frac{1}{12}(1-x^4)\ln^2(x)}{(1-x)\left[-\frac{1}{2}(1+x)\ln(x)-(1-x)\right]^2} \tag{D.8}$$

Appendix E. Statistical diameters calculations

For a given simulation q, the total concentration $N_\mathrm{tot}^{[q]}$, the mode diameter $D_{p,\mathrm{mod}}^{[q]}$, the median diameter $D_{p,50}^{[q]}$, the mean diameter $\overline{D_p}^{[q]}$, the geometric mean diameter $\overline{D_{p,g}}^{[q]}$ and the geometric standard deviation $\sigma_g^{[q]}$ are

computed as follows:

$$N_{\text{tot}}^{[q]} = \sum_{j=1}^{J} \hat{\vec{N}}[j]^{[q]}, \tag{E.1}$$

$$D_{p,\text{mod}}^{[q]} = D_p\left(\max_j \hat{\vec{N}}[j]^{[q]}\right), \tag{E.2}$$

$$D_{p,50}^{[q]} = D_p\left(\frac{N_{\text{tot}}^{[q]}}{2}\right), \tag{E.3}$$

$$\overline{D_p}^{[q]} = \frac{\sum_{j=1}^{J} \hat{\vec{N}}[j]^{[q]} D_p[j]}{N_{\text{tot}}^{[q]}}, \tag{E.4}$$

$$\overline{D_{p,g}}^{[q]} = \exp\left(\frac{\sum_{j=1}^{J} \hat{\vec{N}}[j]^{[q]} \ln(D_p[j])}{N_{\text{tot}}^{[q]}}\right), \tag{E.5}$$

$$\sigma_g^{[q]} = \exp\left(\frac{\sum_{j=1}^{J} \hat{\vec{N}}[j]^{[q]} \left[\ln(D_p[j]) - \ln(\overline{D_{p,g}}^{[q]})\right]^2}{N_{\text{tot}}^{[q]}}\right)^{1/2}. \tag{E.6}$$

Nomenclature

Math symbols

$\circ$	Hadamard product or element-wise product	
$\hat{\lambda}$	Estimate of the regularization parameter	
$\vec{\hat{N}}$	Vector of estimated solution elements	[#.m^{-3}]
$\vec{\hat{N}}_{[\lambda]}$	Vector of estimated solution elements for a given regularization parameter λ	[#.m^{-3}]
λ	Regularization parameter	
$\vec{\vec{H}}_0$	Nominal inversion matrix	
$\vec{\vec{H}}$	Inversion matrix	
$\vec{\vec{I}}_n$	Unit matrix of size n	
$\vec{E}$	Vector of measurement errors	
$\vec{N}$	Vector of solution elements	[#.m^{-3}]
$\vec{w}$	Vector of Simpson quadrature' s weights	
$\vec{Y}$	Vector of measured raw data points	
$\vec{Y}_a$	Vector of actual raw data points	
$\|.\|$	Euclidean norm	
^{T}	Transpose operator	
D_2	Second order finite difference matrix	
I	Number of channels	
J	Number of solution elements	
W	Lambert W function	

SMPS model parameters

(a, b, c)	Constants for slip correction factor calculation	
Δ	Diffusion parameter for a circular tube	
η_0	Reference dynamic gas viscosity at reference temperature T_0	[kg.m^{-1}.s^{-1}]
η_{CPC}	Counting efficiency of the CPC	[%]
η_{DMA}	Penetration efficiency through entrance and exit regions of the DMA	[%]
η_{inlet}	Penetration efficiency through the impactor inlet	[%]
$\eta_{\text{neutralizer}}$	Penetration efficiency through the neutralizer and internal plumbing	[%]
η_{tube}	Penetration efficiency through the tubing to the DMA and CPC	[%]
η_g	Dynamic gas viscosity	[kg.m^{-1}.s^{-1}]
$\lambda_{m,0}$	Reference mean free path for gas molecules at reference temperature T_0 and pressure P_0	[m]
λ_m	Gas molecule mean free path	[m]
$\mathfrak{n}$	Aerosol size distribution	[#.m^{-3}]
ω	DMA transfer function	
ω_{d}	DMA diffusive transfer function	
ω_{nd}	DMA non-diffusive transfer function	
$\overline{\eta}$	Bin averages of the efficiency	[%]
$\overline{\hat{\lambda}}$	Mean estimate of the regularization parameter	
$\overline{\omega_i}$	Classifier mean transfer function through channel i	
$\overline{V(t)}$	Mean voltage for a counting time t	[V]

$\overline{v}$	Mean velocity in the tube	[m.s^{-1}]
$\phi(p, D_p)$	Aerosol charge fraction as a function of the particle mobility diameter D_p and the number of carried charges p	
τ_v	Time constant of the voltage ramp	[s]
τ_{cpc}	Per-event dead time of the CPC	[s]
C_c	Slip correction	
D	Diffusion coefficient of a particle in air	[m^2.s^{-3}]
D_{tube}	Plumbing tube diameter	[m]
D_p	Particle mobility diameter	[m]
k_i	Nonnegative kernel function for the time range corresponding to the channel i	
K_n	Knudsen number	
l	Length of the DMA column	[m]
L_{eff}	Effective tube length	
l_{tube}	Plumbing tube length	[m]
N_{scans}	Number of scans	
P	Gas pressure inside the classifier	[Pa]
p	number of elementary charges	
P_0	Reference gas pressure, P_0 = 101.3 kPa	[Pa]
q_{a}	Aerosol inlet flow rate	[m^3.s^{-1}]
q_{ex}	Excess air outlet flow rate	[m^3.s^{-1}]
q_{m}	Aerosol sampling outlet flow rate	[m^3.s^{-1}]
q_{sh_0}	Set point value for the clean sheath air inlet flow rate	[m^3.s^{-1}]
q_{sh}	Clean sheath air inlet flow rate	[m^3.s^{-1}]
r_1	Outer radius of axial classifier center rod	[m]
r_2	Inner radius of axial classifier housing	[m]
R_{tube}	Plumbing tube radius	[m]
s	Mobility parameter of (Wang and Flagan, 1990)	
T	Gas temperature inside the classifier	[K]
t	Time	[s]
$t[i]$	Arrival time of the particle in channel i	[s]
T_0	Reference gas temperature, T_0 = 296.15 K	[K]
$t_c[i]$	Counting time in channel i	[s]
t_d	Tubing time between the DMA outlet and the CPC detection point	[s]
t_f	Residence time inside the classifier	[s]
t_r	Retrace time	[s]
t_s	Scanning time	[s]
$V(t)$	Voltage as a function of the time	[V]
V_{max}	Maximum voltage for the scan	[V]
V_{min}	Minimum voltage for the scan	[V]
Z	Electrical mobility	[m^2.V^{-1}.s^{-1}]
Z^*	Transfer function centroid electric mobility for a given voltage V	[m^2.V^{-1}.s^{-1}]
Z_d	Particle electrical mobility	[m^2.V^{-1}.s^{-1}]
$\text{erf}(x)$	Gaussian error function, $\text{erf}(x) = \frac{2}{\sqrt{\pi}} \int_0^x \exp(-t^2)dt$	

Ionic properties

$\alpha_p^{\pm}$	Fuchs' parameter: collision probability of small ions (positive and negative) with a particle	

	that represents the fraction of ions emerging from the limiting sphere that actually reach the particle	
$\beta_p^{\pm}$	Attachment coefficient of small ions (positive and negative) with a particle carrying p elementary units of charge (p is considered positive, if the charges of the ion and the particle are of the same sign)	[$m^3.s^{-1}$]
$\delta_I^{\pm}$	Radius of Fuchs' limiting sphere: radius of a sphere that divides the free molecular regime near the particle and the continuum regime far from the particle	[m]
κ	Image force parameter	
$\lambda_I^{\pm}$	Mean free path of small ions (positive and negative)	[m]
ς_p	Electrostatic potential energy of an ion when it moves in the electrostatic field of a charged particle (p being positive if the charges of the ion and the particle are of the same sign)	
$a_i(p)$	Charge fraction matrix coefficients	
b	Impact parameter between the ion and the particle	
$b_{\min}$	Impact parameter of the minimum apsoidal distance	
$D_I^{\pm}$	Diffusion coefficient of small ions (positive and negative) in air	[$m^2.s^{-3}$]
K	Number of listed authors that published values of the ionic properties for dry air	
$m_I^{\pm}$	Mass of small ions (positive and negative)	[amu]
r	Distance of the ion from the center of the particle	
R_p	Aerosol particle radius	[m]
r_a	Apsoidal distance between the ion and the particle	[amu]
$v_I^{\pm}$	Thermal velocity of small ions (positive and negative)	[$m.s^{-1}$]
$z_I^{\pm}$	Electrical mobility of small ions (positive and negative)	[$m^2.V^{-1}.s^{-1}$]
F_{int}	Force of the electrostatic interaction between the ion and the particle	

Statistical modeling

(a_A, b_A, c_A)	Slip correction factors of (Allen and Raabe, 1985)	
(a_H, b_H, c_H)	Slip correction factors of (Hutchins et al., 1995)	
(a_J, b_J, c_J)	Slip correction factors of (Jung et al., 2012)	
(a_K, b_K, c_K)	Slip correction factors of (Kim et al., 2005)	
ΔP	Modeled tolerance around P	
ΔT	Modeled tolerance around T	
Δ_{thres}	Diameter range for the transition between ω_{d} and ω_{nd}	
ϵ_V	Uniform random variable used to scale the voltage ramp	
$\hat{T}$	Uniform random variable that models the gas carrier temperature inside the classifier	
$\hat{V}_{max}$	Gaussian random variable that models the maximum voltage dispersion	
$\hat{V}_{min}$	Gaussian random variable that models the minimum voltage dispersion	
$\mu_{\Phi_{p,\text{samp}}}$	J-dimensional mean vector of $\Phi_{p,\text{samp}}$	
$\overline{\delta}_V$	Mean voltage offset	
$\overline{\eta_0}$	Normal random variable that models the reference gas viscosity	
$\overline{D_{p,g}}$	Geometric mean diameter	[m]
$\overline{D_p}$	Mean diameter	[m]
$\phi_k(p, D_p)$	Bipolar charging law calculated with the k^{th} quadruplet of table 3	
$\Phi_{p,\text{samp}}$	$J \times K$ matrix containing the J-dimensional vectors $\phi_k(p, D_p)$	
Φ_p	Multivariate normal random vector that models the bipolar charging law with p charges	
σ_g	Geometric standard deviation	
$\sigma^2_{\eta_0}$	Variance of $\overline{\eta_0}$	

$\sigma_{\Phi_{p,\text{samp}}}$	J-dimensional standard deviation vector of $\Phi_{p,\text{samp}}$	
$\Sigma_{\theta_{A,B,C}}$	Covariance matrix of $\theta_{A,B,C}$	
$\Sigma_{\vec{Y}}$	Covariance matrix of $\vec{Y}$	
$\Sigma_{C_{\Phi_{p,\text{samp}}}}$	Diagonal matrix with non-negative real numbers known as the singular values of $C_{\Phi_{p,\text{samp}}}$ on the diagonal	
$\theta_{A,B,C}$	Multivariate truncated normal vector containing A, B and C	
$\tilde{\vec{Y}}$	Multivariate normal random vector that models the measured particle count	
$\tilde{\vec{Y}}_{\text{poisson}}$	Multivariate Poisson random vector that models the measured particle count	
A, B, C	Truncated normal variables that models the slip correction factors a, b and c	
$C_{\Phi_{p,\text{samp}}}$	$J \times J$ rank correlation matrix of $\Phi^T_{p,\text{samp}}$	
$D_{p,50}$	Median diameter	[m]
$D_{p,\text{mod}}$	Mode diameter	[m]
$D_{p,\text{thres}}$	Uniform random variable that models the diameter from which the transition from ω_d to ω_nd begins	
$D^{\text{low}}_{p,\text{thres}}$	Lower bound of $D_{p,thres}$	
$D^{\text{up}}_{p,\text{thres}}$	Upper bound of $D_{p,thres}$	
g	Mixing function that handles the transition between ω_d and ω_nd	
L, R_1, R_2	Uniform random variables that model the geometrical parameters of the DMA	
N_{tot}	Total concentration	[#.m^{-3}]
Q	Number of simulations of Monte Carlo	
$Q_{\text{sh}}, Q_\text{a}, Q_\text{m}, Q_{\text{ex}}$	Normal random variables that model the DMA flow rate	
$U_{C_{\Phi_{p,\text{samp}}}}$	Orthogonal matrix or rotation matrix of the singular value decomposition of $C_{\Phi_{p,\text{samp}}}$	

Physical constants

ϵ_0	Vacuum permittivity	[F.m^{-1}]
ϵ_1	Dielectric constant	[F.m^{-1}]
e	Charge of an electron	[C]
k_b	Boltzmann constant	[J.K^{-1}]
M	Average molecular mass of air	[amu]
S	Sutherland constant, $S = 110.4$ K	[K]